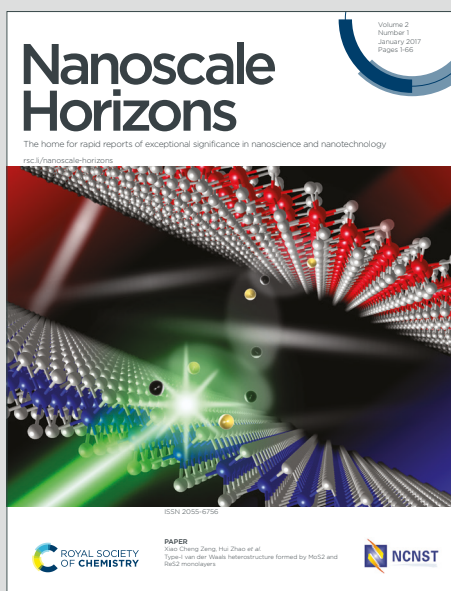


Nanoscale Horizons

The home for rapid reports of exceptional significance in nanoscience and nanotechnology

Accepted Manuscript

This article can be cited before page numbers have been issued, to do this please use: J. Won and A. T. Liu, *Nanoscale Horiz.*, 2026, DOI: 10.1039/D6NH00001K.



This is an Accepted Manuscript, which has been through the Royal Society of Chemistry peer review process and has been accepted for publication.

Accepted Manuscripts are published online shortly after acceptance, before technical editing, formatting and proof reading. Using this free service, authors can make their results available to the community, in citable form, before we publish the edited article. We will replace this Accepted Manuscript with the edited and formatted Advance Article as soon as it is available.

You can find more information about Accepted Manuscripts in the [Information for Authors](#).

Please note that technical editing may introduce minor changes to the text and/or graphics, which may alter content. The journal's standard [Terms & Conditions](#) and the [Ethical guidelines](#) still apply. In no event shall the Royal Society of Chemistry be held responsible for any errors or omissions in this Accepted Manuscript or any consequences arising from the use of any information it contains.

1 From Plant Transpiration to Hydrovoltaics: Distributed Energy Harvesting Driven by 2 Water Evaporation

3 Jongbin Won¹ and Albert Tianxiang Liu^{1,2,3,4,*}

4
5 ¹Department of Chemical Engineering, University of Michigan, Ann Arbor, MI, 48109, USA

6 ²Department of Material Science and Engineering, University of Michigan, Ann Arbor, MI 48109,
7 USA

8 ³Macromolecular Science and Engineering, University of Michigan, Ann Arbor, Michigan 48109,
9 United States

10 ⁴Biointerfaces Institute, University of Michigan, Ann Arbor, MI

11
12 *Corresponding author:
13 Dr. Albert Tianxiang Liu
14 Department of Chemical Engineering
15 University of Michigan
16 Ann Arbor, MI 48109, United States
17 Telephone: +1-734-763-5192
18 E-mail: atliu@umich.edu
19

20 Abstract

21 Evaporation continuously converts absorbed solar heat into the kinetic motion of water
22 molecules, creating a ubiquitous driving force that remains largely untapped for direct electricity
23 generation. In plants, this process is harnessed through transpiration, where capillary flow and
24 sustained negative pressure drive long-range water transport without moving parts. Inspired by
25 this natural hydraulic engine, transpiration-inspired hydrovoltaics (TIH) have emerged as solid-
26 state material platforms that convert evaporation-driven water transport into electrical output
27 through interfacial electrokinetic processes. In this review, we introduce a unified physical
28 framework for TIH by explicitly connecting the physics of plant transpiration to evaporation-
29 driven electricity harvesting in engineered porous media. We summarize the governing principles
30 of water ascent in trees, including capillarity, water-potential gradients and cohesion–tension
31 stability, and map these concepts onto synthetic TIH architectures built from hydrophilic micro-
32 and nanofluidic networks. We critically examine the proposed electricity-generation mechanisms
33 in TIH, including classical streaming potentials on insulating substrates, pseudo-streaming in



34 conductive porous networks and ionovoltaic coupling in semiconducting channels. We synthesize
35 how geometry, pore microarchitecture, surface chemistry, electrical conductivity and
36 environmental conditions such as humidity, temperature and airflow jointly govern device
37 performance. By benchmarking TIH against decades of quantitative insight from plant hydraulics,
38 we identify key trade-offs, unresolved mechanistic questions, and actionable design opportunities
39 for robust, scalable evaporation-driven power generation and self-powered sensing. Together,
40 these perspectives TIH as a promising platform for distributed energy harvesting at the water-
41 energy nexus.

42 **Keywords:** Transpiration, Energy Harvesting, Hydrovoltaics, Nanoporous Materials, Interfacial
43 Phenomena

44

45 1. Introduction

46 Nearly all renewable energy originates from the sun, with the Earth's atmosphere, oceans,
47 and landmasses absorbing approximately **3,850,000 exajoules** annually. Water absorbs and
48 redistributes a large fraction of incoming solar energy, translating to an estimated **60 petawatts**
49 per year,¹ three orders of magnitude greater than the annual global energy consumption. Most of
50 this absorbed energy dissipates as thermal and vibrational energy (molecular motion), driving
51 water evaporation, a spontaneous and continuous phase transition from liquid to vapor that sustains
52 the Earth's water cycle.¹⁻³ It should be noted that water itself contains little intrinsically harvestable
53 chemical energy in its molecular bonds. Instead, the only exploitable energy associated with water
54 comes from the physical (thermal and mechanical) energy it carries. Water serves as the carrier,
55 not the source, of energy that can be harvested.⁴

56 The kinetic energy of water has been exploited for centuries, with early civilizations using
57 water wheels and mills to convert bulk water flow into mechanical power.⁵ Today, hydroelectric
58 power that converts the kinetic energy of collected bulk water flow into electricity using turbines
59 is a major source of renewable electricity. This progression reflects a recurring theme: water's
60 energy has been easiest to harvest when it is organized into large-scale, directed motion. Yet the
61 water cycle begins in almost a completely opposite fashion, namely through highly distributed,
62 molecular-scale evaporation processes occurring across open waters, soils, and vegetation.
63 Consequently, even though a modern turbine can easily convert bulk kinetic energy into electricity



64 with over 90 % efficiency,⁶ less than 0.003% of evaporated water is ever collected inside a
65 reservoir and stored behind a dam.⁷ As a result, the vast thermal energy driving the evaporation
66 process everyday still remains largely untapped.

67 This contrast motivates a simple question: why capture water's energy primarily at the end
68 of the water cycle, after vapor condenses, precipitation occurs, and flow concentrates into rivers,
69 rather than closer to the source of evaporation? From a physics standpoint, evaporation is where
70 thermal input is first converted into nonequilibrium molecular transport. If that dispersed transport
71 could be rectified into electrical output locally, the water cycle would offer an additional, spatially
72 distributed route for energy conversion that complements conventional hydroelectric power.

73 The primary obstacle in harvesting evaporative energy lies in its molecular scale nature.
74 Conventional kinetic-to-electric conversion tools, such as turbines, require concentrated flow and
75 well-defined momentum transfer to operate efficiently. Evaporation-driven transport, by contrast,
76 occurs at the scale of individual water molecules, making it difficult to capture using conventional
77 means.⁸ **A molecular-scale problem calls for a molecular-scale solution.** To harness the kinetic
78 energy of evaporating water molecules, we need to develop nanoscale energy converters, even if
79 they look nothing like their macroscopic counterparts. We need nanoscale architectures that
80 efficiently couple molecular motion to electronic charge transport. This requirement helps explain
81 why direct evaporative energy capture has long remained more of a conceptual opportunity than a
82 widely realized technology.

83 Recent advances in nanomaterials and porous functional media have begun to close this
84 gap.^{9,10} The key advantage of nanomaterials lies in their high surface-area-to-volume ratios, which
85 facilitate molecular-scale interactions necessary for capturing water's kinetic energy. Additionally,
86 nanomaterials exhibit quantum confinement effects¹¹ and strong surface phonon-electron
87 coupling,¹² enhancing direct mechanical-to-electrical energy conversion efficiency from adsorbed
88 molecules. Indeed, these nanostructured solid-state materials have been demonstrated to sustain
89 capillary-driven flow, maintain evaporation at exposed interfaces,¹³ and mediate interfacial charge
90 separation via surface functional groups and electric double layers (EDL).^{14,15} This electrokinetic
91 phenomenon, known as the **hydrovoltaic (HV) effect**, provides a direct means of capturing
92 molecular scale water motion into useable electricity.



93 Nature provides a compelling proof-of-principle that evaporation can sustain persistent
94 transport and do useful work. Through transpiration, plants continuously pump water and nutrients
95 over long distances, often tens of meters, without moving parts. Distributed evaporation at leaves
96 generates and maintains negative pressures in the xylem, while hierarchical porous transport
97 networks and the cohesion–tension stability of water sustain flow under ambient conditions.
98 Importantly for hydrovoltaics, the same features that enable transpiration, including confined water
99 pathways, structured interfaces, and sustained pressure gradients, also create conditions under
100 which interfacial ion transport and charge separation can be amplified and controlled.

101 Motivated by this connection, we use the term **transpiration-inspired hydrovoltaics**
102 **(TIH)** to describe HV systems in which evaporation-driven capillary flow through hydrophilic
103 porous, microfluidic, or nanofluidic networks is central to sustained operation. In TIH devices,
104 porous networks wick water from a reservoir, evaporation drives flow, and interfacial
105 electrokinetic processes convert that flow into electrical output. In this review, we connect
106 transpiration physics to evaporation-driven electricity generation in TIH devices. We first
107 summarize the physical basis of water ascent in trees, then map those principles onto synthetic
108 porous architectures. We examine macroscopic, microscopic, and environmental variables that
109 govern output, discuss the role of electrical conductivity and interfacial chemistry, survey
110 emerging applications, and conclude with key challenges and opportunities for advancing TIH.

111 2. Transpiration Mechanism of Trees

112 Trees regulate water transport by integrating roots, xylem, and stomata into a coupled
113 hydraulic network.¹⁶ Water and dissolved nutrients are taken up from soil, conveyed upward
114 through a hierarchical conduit system, and ultimately released to the atmosphere as vapor through
115 evaporation at the leaves. This sustained ascent of water molecules is remarkable because it occurs
116 without mechanical pumps and routinely overcomes substantial gravitational head. In this section,
117 we summarize the physical basis of transpiration, with emphasis on capillarity, water-potential
118 gradients, and the cohesion–tension framework that rationalizes negative pressure (tension) in
119 xylem water. These concepts provide a foundation for later sections, where evaporation-driven
120 flow in engineered porous networks is coupled to interfacial charge transport in TIH systems.



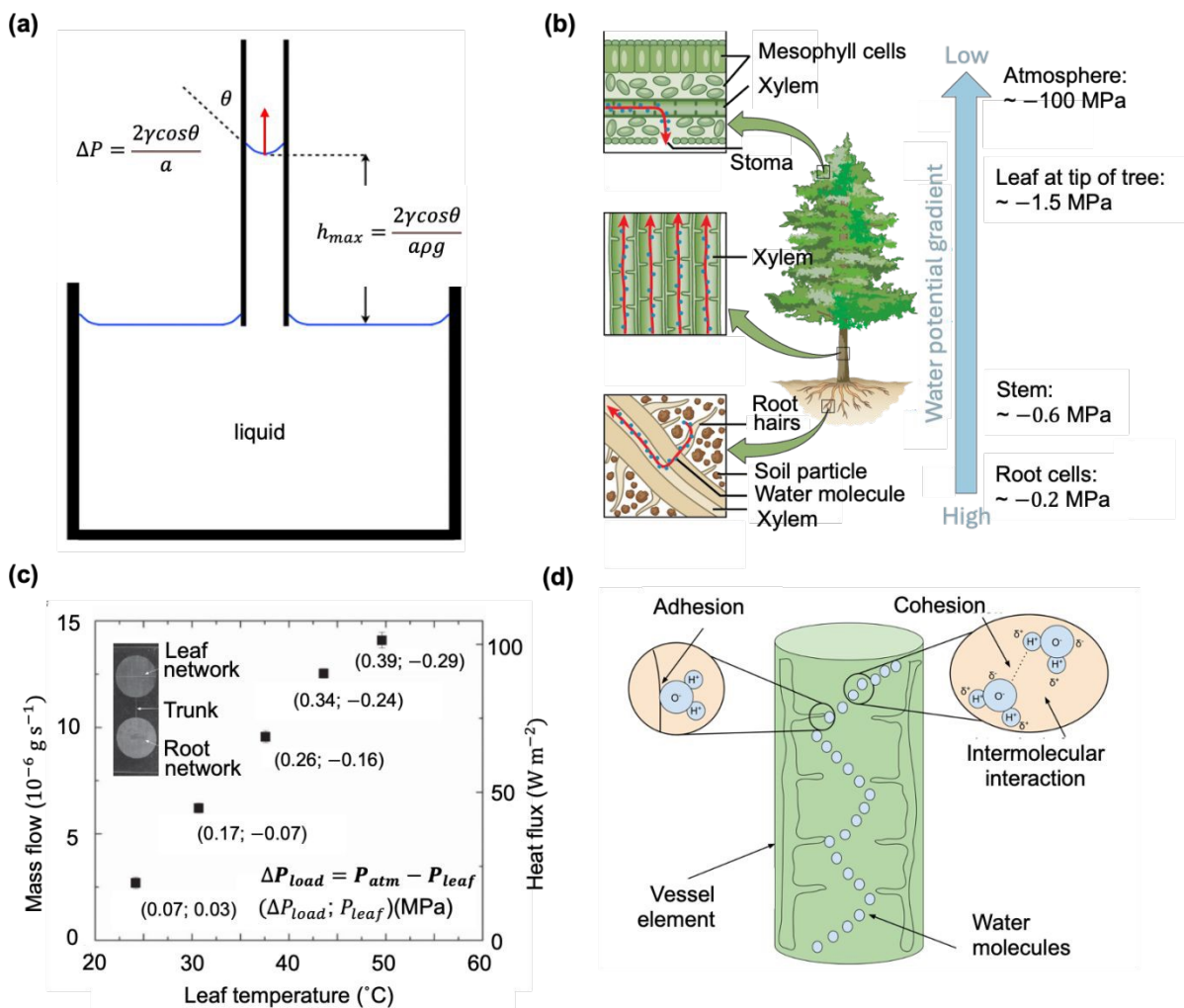


Figure 1. Water ascent in tree driven by negative pressure, as evidenced experimentally and rationalized by the Cohesion-Tension theory.

(a) Capillary rise in a tube connected to a bulk liquid reservoir. The Young–Laplace relation gives the capillary pressure that drives ascent, and the corresponding expression on the right gives the maximum rise height against gravity. Reproduced with permission.¹⁷ Copyright 2025, Elsevier. (b) Schematic illustration of transpiration through root, xylem, and stoma driven by water potential gradient. Reproduced with permission.¹⁸ Copyright 2023, Academic Senate for California Community Colleges OER Initiative (ASCCC OERI). (c) Direct measurement of negative pressure in a hydrogel-based synthetic tree. Inset: photograph of the device comprising a root network, trunk, and leaf network. Reproduced with permission.¹⁹ Copyright 2008, Springer Nature. (d) Cohesion–tension mechanism. Water molecules (blue circles) maintain a continuous liquid column through adhesion to the vessel walls and cohesion between neighboring molecules. Reproduced with permission.¹⁸



121

122

123

124

125

126

127

128

129

130

131

132

133

134 Copyright 2023, Academic Senate for California Community Colleges OER Initiative (ASCCC
135 OERI).

136

137 2.1 Mechanism of capillary rise and its limitation

138 Capillary action is a widely recognized driver of water rise in narrow channels. When water
139 contacts a hydrophilic pore or tube, wetting and surface tension form a curved meniscus at the
140 liquid–air interface. The resulting curvature produces a pressure difference across the meniscus
141 that, for an idealized cylindrical capillary, can be approximated by the Young–Laplace relation:

$$\Delta P = \frac{2\gamma\cos\theta}{a} \quad (1)$$

142 where ΔP is the pressure difference between the liquid and gas phases, γ is the surface tension of
143 water, θ is the contact angle between water and the tube wall, and a is the capillary radius.
144 Capillary rise proceeds until this capillary pressure balances the hydrostatic pressure associated
145 with a liquid column of height h :

$$\rho gh = \frac{2\gamma\cos\theta}{a} \quad (2)$$

146 where ρ is the density of water, g is the gravitational acceleration. Combining Equations (1) and
147 (2) yields the maximum capillary rise height:

$$h_{max} = \frac{2\gamma\cos\theta}{a\rho g} \quad (3)$$

148 This scaling is useful for back-of-the-envelope estimates. Assuming perfect wettability
149 ($\theta = 0$), a tube radius of 10 μm , and using the surface tension and density of water at 25 $^{\circ}\text{C}$, the
150 maximum capillary rise is estimated to be $h_{max} \approx 1.5 \text{ m}$. This is far below the height of many
151 trees and orders of magnitude below the tallest species that exceed 100 m. At the same time,
152 Equation (3) implies that capillary rise can become extremely large as the characteristic pore radius
153 shrinks. For example, if the tube diameter decreases to 10 nm, the same estimate gives h_{max}
154 $\approx 1500 \text{ m}$, illustrating that Young–Laplace pressures can be extremely large under nanoscale
155 confinement.



156 However, predicted heights from Equation (3) do not automatically translate into stable,
157 continuous water columns at those heights. In ordinary conduits under atmospheric pressure, even
158 when an external pump pulls water upward, water columns substantially above about 10 m are
159 difficult to sustain because the liquid enters a tensile state ($\Delta P > 1$ atm in magnitude) and
160 cavitation can nucleate.^{20,21} Once gas nuclei or vapour bubbles form, the water column breaks and
161 the tensile state collapses. The discrepancy between simple capillary-rise estimates and the water
162 ascent observed in trees indicates that additional physics beyond static capillarity is required,
163 specifically the generation and maintenance of negative pressure (tension) in a continuous liquid
164 column while suppressing cavitation.¹⁷

165 2.2 Driving force of water ascent

166 In plant physiology, water movement is commonly described in terms of **water potential**
167 (Ψ), which represents the chemical potential energy of water per unit mass. When expressed in
168 pressure units by incorporating the density of water, Ψ can be interpreted as an effective pressure.
169 Water flows from regions of higher to lower potential. The total water potential is often
170 decomposed into four primary components:

$$\Psi = \psi_{osmosis} + \psi_{gravity} + \psi_{matrix} + \psi_{pressure} \quad (4)$$

171 where $\psi_{osmosis}$ is the osmotic potential arising from solute concentration differences across
172 semipermeable membranes, $\psi_{gravity}$ is the gravitational potential reflecting the influence of
173 gravity on water flow, ψ_{matrix} is the matrix potential associated with interactions between water
174 and solid surfaces, and $\psi_{pressure}$ is the pressure potential associated with hydrostatic pressure
175 within the hydraulic pathway.²² Capillary pressure, introduced in subsection (a), can be
176 incorporated into ψ_{matrix} through the local curvature of liquid–air interfaces within pores.

177 In plants, a sustained water potential gradient is established along the soil–plant–
178 atmosphere continuum. A common qualitative ordering is:

$$\Psi_{soil} > \Psi_{root} > \Psi_{xylem} > \Psi_{leaf} > \Psi_{air} \quad (5)$$

179 where each subscript represents the total water potential in the soil, root, xylem, leaf, and air,
180 respectively.¹⁹ Evaporation at the leaf surface lowers the local water potential by withdrawing
181 water from confined interfacial regions. This maintains a driving force as long as water supply and



182 evaporative demand persist, sustaining continuous flow from soil uptake through root membranes
183 to evaporation through stomata. Remarkably, in many plants, the absolute water potential within
184 the xylem and leaves can reach strongly negative values while water remains liquid. Reported leaf
185 water potentials can approach several negative megapascals relative to soil, despite atmospheric
186 pressure being approximately 0.1 MPa.^{23,24} These observations reinforce that the plant hydraulic
187 system does not operate near atmospheric pressure. Instead, it operates under tension.

188 2.3 Absolute negative pressure confirmed in synthetic tree systems

189 Negative pressure states have been demonstrated not only in living trees^{25–27} but also in
190 synthetic systems that mimic transpiration-driven transport under controlled geometry and
191 boundary conditions.^{19,28} A widely cited example is the synthetic tree developed by Wheeler and
192 Stroock.¹⁹ In that study, a hydrogel-based, unidirectional microchannel network was fabricated in
193 poly(2-hydroxyethyl methacrylate) (pHEMA) using soft lithography. The structure consisted of
194 two bundles of straight microchannels representing the root and leaf networks, interconnected by
195 a single microchannel of approximately 10 μm in diameter that served as the trunk. Water was
196 supplied to the root network, transported through the trunk, and delivered to the leaf network. The
197 root and trunk regions were sealed, whereas the leaf network was exposed to air, thereby localizing
198 evaporation to the leaf-side interface.

199 The volumetric flow rate from the root to the leaf network was measured, and the
200 corresponding pressure drop was inferred using Poiseuille's law for laminar flow through a
201 cylindrical channel:

$$\Delta p = \frac{8\mu L Q}{\pi R^4} \quad (6)$$

202 where Δp is the pressure difference between the root and leaf networks, μ is the dynamic viscosity
203 of water, L is the channel length from the root inlet to the leaf region, Q is the volumetric flow rate,
204 and R is the channel radius. Using measured Q and the known trunk geometry, the calculated
205 pressure at the leaf network was approximately 1 MPa lower than at the root network,
206 corresponding to an absolute negative pressure in the liquid. The boundary condition is clear:
207 evaporation at the exposed leaf network generates a pressure drop that is transmitted through a
208 connected hydraulic pathway. Consistent with this interpretation, simulations predict that
209 pressures below -1 MPa can arise when water flows through micron-scale channels and



210 evaporates into air.²⁹ Together, these results support the physical plausibility of MPa-scale tension
211 in confined liquid pathways sustained by evaporation.

212 **2.4 Cohesion–tension theory explains the negative pressure in water during transpiration.**

213 It is counterintuitive that water can remain liquid under absolute negative pressure, since
214 water typically vaporizes under low-pressure conditions. The cohesion–tension (C–T) theory
215 resolves this by proposing that water in xylem conduits forms a continuous column stabilized by
216 cohesive hydrogen bonding between molecules and adhesive interactions with conduit walls.³⁰ At
217 the leaf surface, evaporation through stomata withdraws water from confined interfacial regions
218 and lowers the local water potential. This creates a tensile force that pulls on the continuous water
219 column. Because cohesion maintains molecular connectivity, this tension propagates downward
220 through the xylem, drawing water upward from the roots.

221 A defining feature of the C–T framework is that xylem water exists in a metastable tensile
222 state.^{31,32} This metastability enables water to remain liquid even when the pressure drops below
223 atmospheric pressure and, in some cases, below zero on an absolute pressure scale. As a result,
224 water can be transported to heights far exceeding the capillary-rise scale suggested by Equation
225 (3). At the same time, the tensile state is not unbounded. If the pressure becomes sufficiently
226 negative, water can cavitate and bubbles can form within xylem conduits, leading to embolisms
227 that reduce hydraulic conductivity.^{19,33,34} Cavitation is therefore widely viewed as a key constraint
228 on water ascent and on the operating envelope of transpiration under high evaporative demand.

229 Several studies have attempted to relate evaporation-associated mass flux to interfacial
230 liquid pressure using kinetic expressions for phase change. One form that has been used is:

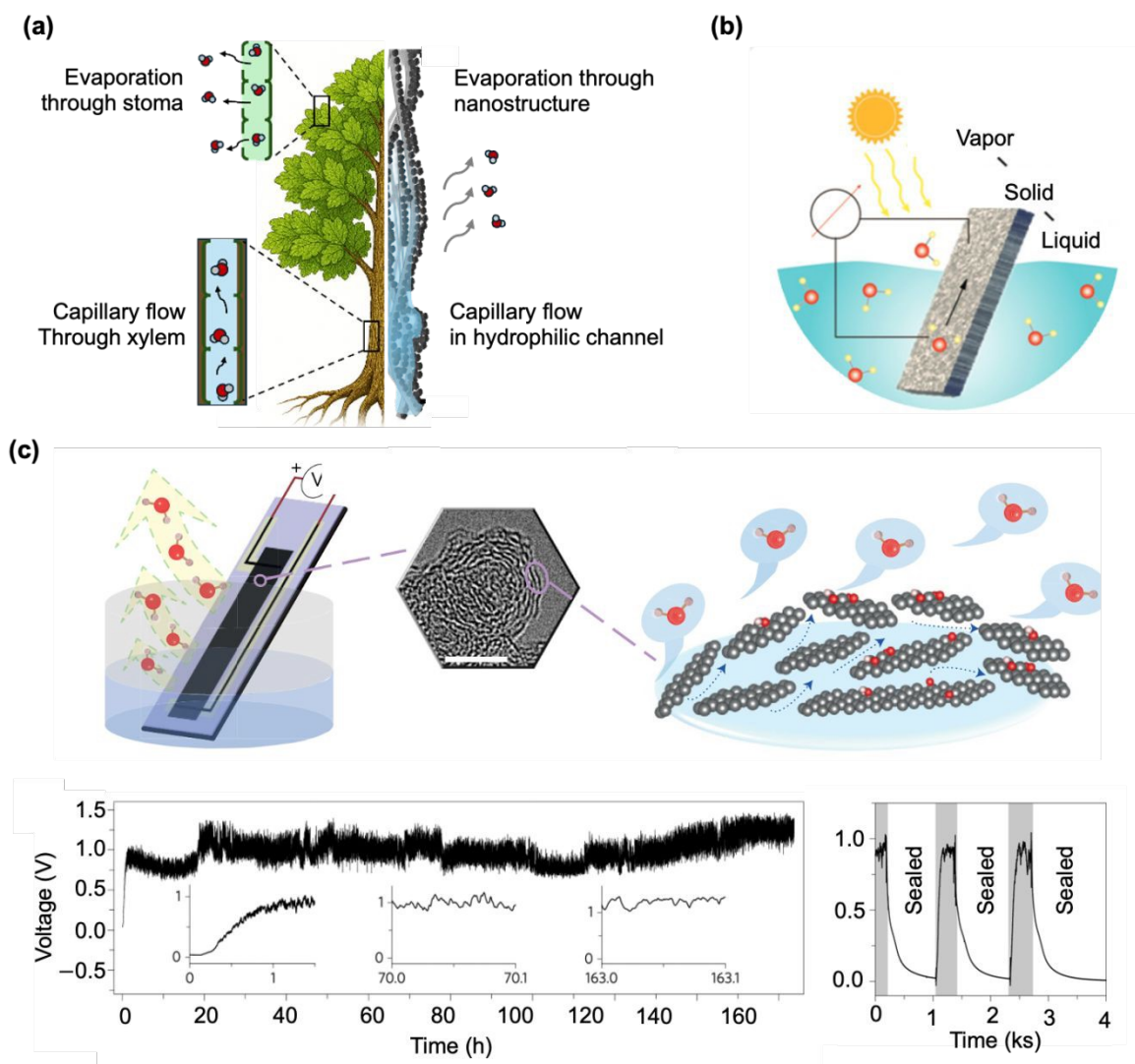
$$\dot{m}_e = \frac{2\sigma}{2 - p_v} \sqrt{\frac{M}{2\pi R} \left(\frac{p_l}{\sqrt{T_l}} - \frac{P_v}{\sqrt{T_v}} \right)} \quad (7)$$

231 where \dot{m}_e is the evaporation mass flux, σ is the accommodation coefficient, M is the molar mass
232 of the fluid, R is the ideal gas constant, p_l is the liquid pressure at the liquid–air interface, P_v is
233 the saturated vapor pressure, T_l and T_v are the liquid temperature and saturated vapor temperature,
234 respectively.³⁵ With a sign convention in which \dot{m}_e is defined as the outgoing flux from water to
235 air, \dot{m}_e is negative during evaporation. When other variables are approximately constant, this



236 expression indicates that p_l is coupled to \dot{m}_e , linking the evaporative flux at the vapor–liquid
 237 interface to the local liquid pressure. In this way, evaporation continuously regenerates the
 238 negative pressure needed to sustain upward transport, thereby closing the transpiration cycle.

239 3. Transpiration-Inspired Hydrovoltaics: A New Energy Harvesting Paradigm



240
 241 **Figure 2. Emergence of transpiration-inspired electricity harvesting enabled by hydrophilic**
 242 **micro-/nano-capillary architectures.** (a) Analogy between natural transpiration and “artificial
 243 tree” devices used for electricity generation. The left schematic depicts water uptake and ascent
 244 through xylem and evaporation through stomata, the two functional elements most directly
 245 emulated in TIH. The right schematic illustrates how hydrophilic channels can replace xylem,
 246 while nanostructured media at an exposed surface sustain evaporation in a stomata-like manner.



247 **(b)** Schematic illustration of a transpiration-inspired hydrovoltaic (TIH) device. Liquid water
248 wicks through a hydrophilic porous matrix and evaporates to vapor at the exposed interface;
249 electrodes placed at two ends across the solid matrix measure a voltage and sustain an electric
250 current through an external circuit. Reproduced with permission.⁵ Copyright 2022, Royal Society
251 of Chemistry. **(c)** Representative TIH implementation using nanostructured carbon. A carbon-
252 black film (black region) deposited on a substrate (blue) comprises interconnected nanopores
253 (TEM image). Upon partial immersion, water infiltrates the porous network and continuously
254 evaporates from exposed regions, producing a sustained electrical output (bottom left). Sealing the
255 device suppresses evaporation and extinguishes the voltage (bottom right), supporting an
256 evaporation-sustained generation mechanism. Reproduced with permission.³⁶ Copyright 2017,
257 Springer Nature.

258
259 For a long time, harnessing the water cycle through transpiration was exclusive to plants.
260 Recent advances in nanomaterials and microfabrication have enabled synthetic, tree-like systems
261 built from hydrophilic micro- and nanoporous structures that reproduce the key functional
262 elements of transpiration: capillary forces draw water through confined channels, while
263 evaporation at an exposed surface sustains continuous flow, consistent with the cohesion–tension
264 framework. Building on this analogy, transpiration-driven water transport has been repurposed not
265 only for fluid delivery but also for electricity generation. By maintaining a water-potential gradient
266 along the channel and connecting electrodes at the “root” (bottom) and “leaf” (top) regions, a
267 potential difference can develop across the device and drive current through an external circuit.

268 **3.1 Advent of transpiration-inspired hydrovoltaics and operating principle**

269 This concept is realized in hydrovoltaics (HV), an emerging class of technologies that
270 generate electricity from interactions between water (or aqueous electrolytes) and solid
271 substrates.^{5,14,37,38} Transpiration-inspired architectures are particularly compelling because they
272 can sustain continuous, relatively stable output under ambient conditions. To mimic plant water
273 transport, TIH devices are constructed from hydrophilic networks with micro- and nanoscale
274 confinement, including natural wood templates, engineered porous membranes, and assemblies of
275 organic or inorganic micro- and nanoparticles. These networks are implemented as thin films on
276 substrates or as free-standing porous matrices. In a canonical configuration, one end of the film or



277 matrix is immersed in a water reservoir so that capillarity wicks liquid into the pore network, while
278 evaporation from exposed surfaces maintains flow. Under these conditions, a voltage and current
279 can develop between the immersed region and the evaporating region, reflecting the coupling of
280 flow, ion redistribution, and interfacial charge separation along the porous pathway.

281 **3.2 Early demonstrations and electrokinetic interpretation**

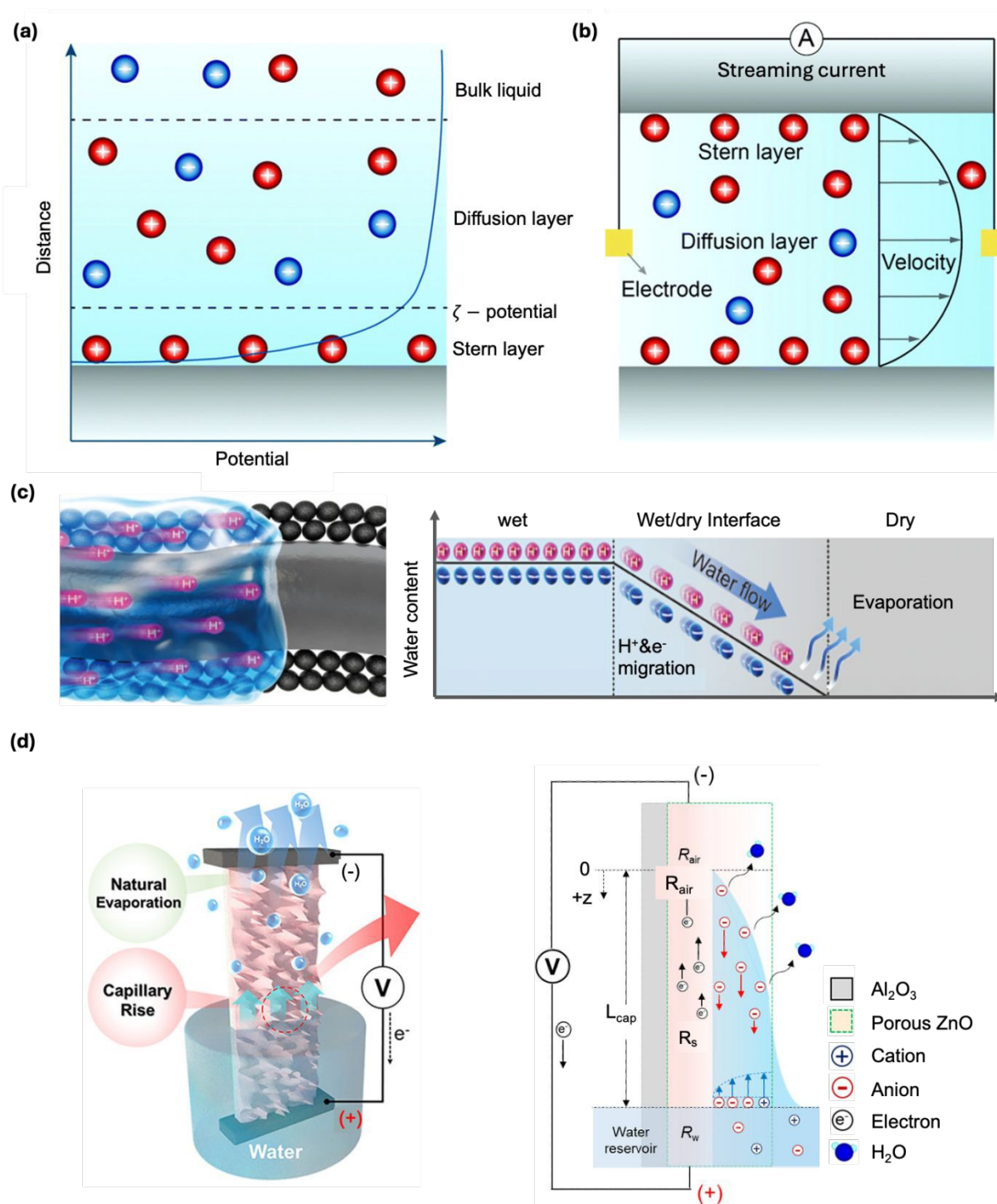
282 One of the early demonstrations of HV power generation was reported in 2017 by Xue et
283 al. using a nanostructured carbon device. In their approach, a carbon-soot film was deposited on a
284 glass substrate (for example, by ethanol-flame deposition), rendered hydrophilic, and connected
285 by carbon nanotube electrodes near its top and bottom edges.³⁶ When the bottom edge was
286 submerged in deionized water, capillary infiltration through the nanoporous network drew liquid
287 upward, while evaporation to air sustained the flow. This, in our view, closely mirrors the
288 functional logic of plant transpiration, at least in part. The device produced an output on the order
289 of volts and maintained a stable signal for extended operation, reported to exceed 160 hours. A
290 particularly informative observation was the strong dependence on evaporation. When evaporation
291 was suppressed (for example by sealing the system so that local relative humidity approached
292 100%), the voltage rapidly vanished. When the system was reopened and evaporation resumed,
293 the output was restored. This reversibility directly implicates evaporation as essential not only for
294 initiating but also for maintaining steady power generation.

295 Mechanistically, the original interpretation invoked classical electrokinetic concepts, such
296 as streaming current and streaming potential, which naturally connect pressure- or capillarity-
297 driven flow in charged confinement to an electrical potential difference. At the same time, the
298 detailed physics remained incompletely resolved. Around the same period, Liu, Kunai and co-
299 workers reported evaporation-driven electricity generation in single-walled carbon nanotube
300 devices using polar organic solvents such as acetonitrile³⁹ and alcohol.⁴⁰ Although such solvents
301 are less ubiquitous than water, these studies were valuable in shaping early mechanistic thinking
302 and highlighting the importance of liquid saturation asymmetry in evaporation-driven power
303 generation.⁴¹ Subsequent studies have shown that multiple mechanisms can contribute, depending
304 on material composition, pore morphology, ionic strength, and whether the device operates in a
305 sustained-flow regime or a transient wet–dry asymmetry regime. We summarized several key
306 mechanisms proposed in the following section.



307 4. Mechanism of Electricity Transduction in TIH Devices

308 4.1 Electrokinetic mechanisms



309

310 **Figure 3. Electrokinetic routes for electricity generation in TIH devices.** Mechanisms are

311 grouped into three conceptual classes: classical streaming, pseudo-streaming in conductive porous



312 channels, and ionovoltaic transduction in semiconducting frameworks. **(a, b)** Electric double layer
313 (EDL) at a negatively charged solid surface (grey) and the classical streaming-current/streaming-
314 potential mechanism. Cations and anions are shown as red and blue circles, respectively; the blue
315 curve denotes the electrostatic potential versus distance from the surface. Reproduced with
316 permission.⁵ Copyright 2022, Royal Society of Chemistry. **c)** Pseudo-streaming (PS) mechanism
317 in an electronically conductive porous medium. Protons (red) and electrons (blue) are depicted
318 schematically; conductive carbon-black nanoparticles (black) are deposited on a hydrophilic
319 cellulose fabric. Water infiltration and evaporation (white–blue arrows) are proposed to couple
320 interfacial ion motion to electron transport within the percolated carbon network. Reproduced with
321 permission.⁴² Copyright 2019, American Chemical Society. **d)** Ionovoltaic mechanism. In contrast
322 to the PS picture, a diffusion/electrodifusion flux opposing the convective ion transport
323 (analogous to the conduction current in classical streaming) is proposed to drive an electronic
324 response in the solid via interfacial Coulombic coupling. Reproduced with permission.⁴³ Copyright
325 2019, American Chemical Society.

326

327 4.1.1 Electric double layer formation at charged solid–electrolyte interfaces

328 Several theoretical frameworks have been proposed to describe electricity generation in
329 TIH devices. Despite differences in emphasis, most models share a common electrokinetic
330 foundation: formation of an electric double layer (EDL) at the interface between a charged solid
331 surface and an electrolyte.⁴⁴ Many solids acquire surface charge through ionization of functional
332 groups or specific ion adsorption; in plants, xylem walls are typically negatively charged. The
333 resulting interfacial charge attracts counterions and repels co-ions, producing an asymmetric ion
334 distribution near the surface. The EDL is commonly described as a compact Stern layer, where
335 counterions are strongly associated with the surface, and a diffuse layer, where counterions extend
336 into the solution with weaker association.

337 When capillary pressure (or other pressure gradients) drives liquid through a charged
338 micro- or nanochannel, counterions in the diffuse layer are advected along the channel. This
339 selective interfacial ion transport can generate an axial electric field and a potential difference
340 between channel ends. How that ionic motion is converted into a sustained electronic current
341 depends on the detailed device property and architecture: whether charge conversion occurs



342 primarily at electrodes through Faradaic reactions across an electrically insulating substrate, within
 343 an electronically conductive porous solid, or through interfacial coupling to carriers in a
 344 semiconducting material.

345 **4.1.2 Streaming potential from pressure-driven EDL transport across electrically insulating** 346 **substrates**

347 Among the electrokinetic explanations proposed for TIH devices, the most established is
 348 the classical streaming potential mechanism.^{45–48} In this framework, pressure-driven flow through
 349 a charged channel convects excess countercharge in the diffuse layer, producing an ionic streaming
 350 current; under open-circuit conditions, charge separation builds an opposing electric field that
 351 yields a measurable streaming potential. Formally, the phenomenon is captured by coupled
 352 continuum descriptions of flow and charge transport (for example, Navier–Stokes/Stokes for
 353 hydrodynamics coupled with Poisson–Nernst–Planck for electrostatics and ion migration), which
 354 together describe how interfacial charge, flow, and ionic flux co-evolve in confined electrolytes.

355 As liquid moves through a charged channel, the net charge density in the diffuse layer is
 356 advected, producing the ionic streaming current I_{str} :

$$I_{str} = \int_{-R}^R \rho_e(r) v_x(r) dr \quad (8)$$

357 where $\rho_e(r)$ is the local volumetric charge density in the EDL, $v_x(r)$ is the axial velocity profile,
 358 and R denotes the characteristic radial length scale of the channel. A defining assumption of the
 359 classical picture is that the channel walls are electrically insulating, so the convected ionic current
 360 cannot, by itself, constitute a sustained electronic current through an external circuit. Instead,
 361 conversion between ionic and electronic current must occur through Faradaic charge-transfer
 362 reactions at the electrodes (often implemented using redox couples such as Ag/AgCl). If the
 363 external circuit is open (or highly resistive), continuous Faradaic conversion is impeded. Charge
 364 therefore accumulates, building an electric field along the channel that drives an opposing, field-
 365 driven ionic current typically described as a conduction current I_{cond} :

$$I_{cond} = \int_0^R \kappa dr \quad (9)$$



366 where κ is the electrolyte conductivity. Under open-circuit conditions, At steady state under open
367 circuit conditions, the currents balance, $I_{str} + I_{cond} = 0$, and the resulting streaming potential
368 satisfies:

$$V_{str} = I_{str}R_{solution} \quad (10)$$

369 where $R_{solution} = \kappa^{-1}$ is the effective solution resistivity. Applying the parallel-plate
370 approximation (and under standard electrokinetic assumptions), this reduces to the familiar
371 relation:

$$V_{str} = \frac{\varepsilon_0 \varepsilon_r \zeta}{\mu \kappa} \Delta p \quad (11)$$

372 where $\varepsilon_0 \varepsilon_r$ is the electrolyte permittivity, ζ is the zeta potential, μ is viscosity, and Δp is the
373 pressure drop along the channel. Equation 11 yields several core design intuitions relevant to TIH.
374 First, V_{str} increases with stronger interfacial charge (larger ζ) and larger driving pressure Δp . In
375 TIH devices, Δp is often supplied by capillary pressure, which increases as the characteristic pore
376 radius decreases (Equation 1). This coupling suggests that smaller pores can, in principle, support
377 larger streaming potentials, provided that the channel remains sufficiently permeable to sustain
378 flow. Second, V_{str} decreases with increasing electrolyte conductivity κ , a trade-off that is closely
379 related to EDL screening. At higher ionic strength, the Debye length shrinks to the nanometer scale,
380 compressing the diffuse layer and reducing the degree of counterion selectivity within the channel,
381 thereby suppressing streaming-potential generation.⁴⁹ Consistent with this expectation, Xue et al.
382 reported a decrease in voltage at higher salt concentrations and attributed the trend to Debye
383 screening that weakens EDL-mediated selective ion transport.³⁶ In TIH, evaporation does more
384 than initiate capillary uptake: it continuously maintains a pressure gradient (and thus Δp) by
385 sustaining capillary replenishment, analogous to transpiration in plants. Within the classical
386 electrokinetic streaming framework, evaporation therefore stabilizes Δp , supporting a persistent
387 I_{str} and a sustained V_{str} , so long as a stable wetted pathway and interfacial charge are maintained.

388 A key caveat, however, is that the classical streaming-potential mechanism is
389 fundamentally formulated for insulating channels and typically presumes electrode redox
390 chemistry to close the circuit and convert ionic current into electronic current. Many TIH reports
391 instead employ electronically conductive porous networks (for example, carbon-based films) and



392 observe sustained current output without explicit redox couples. These observations motivate
393 “modern” alternative mechanisms in which the conductive channel itself participates in charge
394 transport and the coupling between ionic motion and electronic carriers becomes essential, which
395 we discuss next.

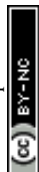
396 4.1.3 Pseudo-streaming in electronically conductive porous channels

397 To rationalize sustained current generation in hydrovoltaic devices that lack explicit redox
398 couples, Kim and co-workers proposed a pseudo-streaming (PS) mechanism in which electronic
399 carriers in a percolated conductor migrate in response to ion motion within the EDL. In their 2019
400 study using a carbon black-coated cotton fabric, the authors argued that voltage generation is
401 primarily interfacial, whereas current generation is transport-driven.⁴² Specifically, spontaneous
402 adsorption of cations onto the negatively charged carbon surface was proposed to establish a built-
403 in potential that can be approximated using a Stern-layer parallel plate capacitor model:

$$V_{EDL} = \frac{\delta\sigma}{\epsilon_0\epsilon_r} \quad (12)$$

404 where V_{EDL} is the built-in voltage induced by adsorbed ions, δ is the Stern-layer thickness, and σ
405 is the effective surface charge density. Their solvent controls supported the role of ionizable
406 species: protic liquids produced voltage, whereas a polar aprotic solvent (propylene carbonate)
407 produced no signal unless LiCl was added, implicating ions and their interfacial organization as
408 essential.

409 Within this framework, current arises when capillary-driven wetting produces a spatially
410 localized EDL and simultaneously drives ion transport. As the wetting front advances through the
411 porous conductor, counterions in the diffuse layer are advected; electrons in the conductive carbon
412 network are proposed to migrate in response, preserving local electroneutrality and producing a
413 measurable current. They termed this output a pseudo-streaming current I_{pst} because, according
414 to their interpretation, its direction is opposite to that expected for the classical streaming current
415 under comparable pressure-driven flow in capillaries of the same sign of surface charge. This
416 directional distinction was presented as an experimentally falsifiable feature that could help
417 discriminate between pseudo-streaming and classical streaming behaviors across different systems.



418 Sustained voltage in the PS picture requires spatial asymmetry in wetting: one end of the
419 device is wetted and supports EDL formation and ionic transport, whereas the opposite end
420 remains comparatively dry and lacks a comparable interfacial ionic structure. This wet–dry
421 asymmetry creates a potential difference between the two ends and persists only while the
422 asymmetric state is maintained. If the porous network becomes uniformly wetted, the EDL-related
423 potentials at the two electrodes are expected to equilibrate and the voltage collapses. Evaporation
424 plays a stabilizing role by continuously removing water from regions away from the wetting site,
425 thereby helping maintain the spatial potential gradient and enabling longer-lived output under
426 ambient conditions.

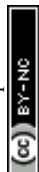
427 A qualitative scaling relation for the pseudo-streaming current has been suggested:

$$I_{pst} \propto Q\sigma s \quad (13)$$

428 where Q is flow rate and s is a characteristic separation length capturing the spatial extent of wet–
429 dry asymmetry and/or charge separation.⁵⁰ This form captures intuitive dependencies, namely that
430 stronger capillary transport (larger Q) and stronger interfacial charge (larger σ) should increase the
431 current magnitude, suggesting design routes that increase hydrophilicity, reduce flow resistance,
432 and enhance surface ionization. However, the relation remains phenomenological. A quantitative
433 framework that couples partially saturated flow, evolving EDL structure, and the simultaneous
434 ionic and electronic conductivities of the porous conductor is still needed to predict how I_{pst} and
435 the associated voltage scale with pore geometry, electrolyte composition, and evaporation rate.

436 4.1.4 Ionovoltaic mechanisms in semiconducting channels

437 A complementary class of mechanisms emphasizes coupling between evaporation-driven
438 ionic polarization in the liquid and charge carriers transport in semiconducting solids. In 2019,
439 Yoon et al. introduced an ionovoltaic mechanism, in which evaporation-driven ionic accumulation
440 generates a local electric field that modulates carrier transport within the solid channel.⁴³ The
441 central idea is that ion accumulation near the evaporating edge polarizes the electrolyte, and the
442 resulting field drives an electronic response in the semiconducting framework through Coulombic
443 coupling at the solid–liquid interface. In their initial demonstration using aluminium-doped zinc
444 oxide (ZnO:Al), the positively charged surface preferentially attracts anions. Capillary flow
445 convects anions upward (I_{conv} , blue arrow in the schematic), while evaporation enriches ions near



446 the capillary edge, producing spatial ionic polarization. This polarization generates a local electric
447 field along the ZnO channel that drives an opposing diffusion or electro-diffusion flux I_{diff} (red
448 arrow), conceptually analogous to the counter-current that balances convection in classical
449 streaming. Through interfacial Coulombic interactions, the anion back flux I_{diff} is proposed to
450 induce a compensating electronic response in the semiconducting channel to maintain local
451 electroneutrality, giving rise to an electronic current I_s (measured as the device output). An Ohmic
452 relationship between measured current and voltage was reported, $V_s = I_s R_s$, where R_s is the
453 effective electrical resistance of the ZnO channel.

454 Subsequent work extended this concept to other materials. In 2021, the same group
455 reported supporting evidence using SiO₂ and MoS₂ nanoflake channels.⁵¹ Because their surfaces
456 are negatively charged, cations are selectively transported, and the output polarity reverses relative
457 to ZnO:Al. To probe ion enrichment directly, NaCl was added and the spatial sodium distribution
458 was quantified by X-ray photoelectron spectroscopy (XPS), revealing stronger Na signal near the
459 upper region of the device, consistent with evaporation-driven accumulation at the capillary edge.
460 On this basis, the authors argued that continuous evaporation maintains localized enrichment,
461 sustaining an electric field and a dynamic balance between convective transport and back-diffusion
462 that continuously couples to electronic transport in the semiconducting network.

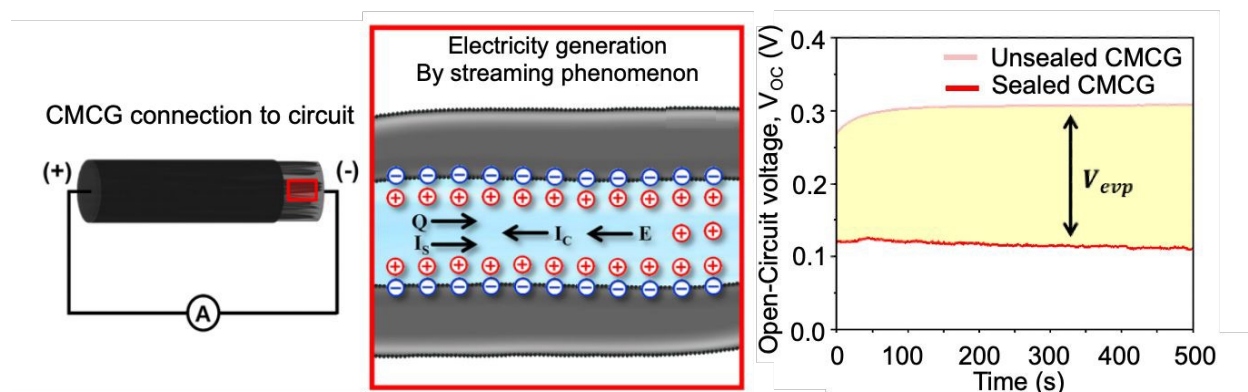
463 Conceptually, ionovoltaic and pseudo-streaming mechanisms share a common theme:
464 ionic motion in the liquid couples to electronic current in the solid. The proposed driving force for
465 the electrical current, in the case of ionovoltaics, is an evaporation-sustained electric field arising
466 from ion accumulation and concentration gradients along a semiconducting channel. Although
467 spatial ion enrichment has been experimentally observed, a major gap remains a quantitative
468 framework that links the measured ionic concentration profile (and its evolution under evaporation)
469 to the resulting electric field and to the magnitude and scaling of I_s and V_s along the channel.

470 **4.2 Importance of evaporation**

471 Beyond sustaining continuous operation, multiple studies suggest that evaporation can also
472 increase the magnitude of the voltage and current produced by TIH devices. In other words,
473 evaporation can act not only as the engine that maintains capillary replenishment, but also as an
474 effective amplifier of the electrical output.

475





476

477 **Figure 4. Role of evaporation in enhancing TIH power output.** Left, circuit schematic for the
 478 cellulose microfiber cylindrical generator (CMCG). The dark region denotes the wetted segment,
 479 whereas the shaded region denotes the comparatively dry segment, establishing a longitudinal wet–
 480 dry asymmetry. Middle, microscopic view of the streaming-current framework: capillary-driven
 481 flow Q advects excess countercharge to generate a streaming current I_S ; the induced electric field
 482 E drives an opposing conduction current I_C . Right, measured open-circuit voltage under sealed
 483 (evaporation suppressed) and unsealed (evaporation allowed) conditions; V_{evp} denotes the voltage
 484 increment associated with evaporation. Reproduced with permission.⁵² Copyright 2023, Elsevier.

485

486 Youm et al. examined this effect using a carbon black coated cellulose acetate microfiber
 487 cylindrical generator.⁵² Carbon black nanoparticles were deposited onto a porous cellulose
 488 microfiber cylinder to form the active HV element, and electrodes were attached at both ends. A
 489 water droplet delivered near the positive electrode initiated infiltration and capillary-driven
 490 transport through the porous network, establishing a longitudinal wetting gradient along the
 491 cylinder. Using a streaming-potential framework with empirical pore-scale parameters (including
 492 an average pore size), the authors estimated an open-circuit voltage of approximately 75 mV. To
 493 isolate the role of evaporation, the device was first sealed to suppress water loss. Under sealed
 494 conditions, the measured voltage was about 120 mV, broadly consistent with the estimate given
 495 the uncertainties associated with pore geometry, surface charge, and effective conductivity in a
 496 heterogeneous porous medium. Strikingly, when the device was unsealed and evaporation was
 497 permitted, the open-circuit voltage increased to approximately 310 mV, nearly three times higher
 498 than the sealed value. This result indicates that evaporation does more than sustain flow: it can
 499 intensify the interfacial and transport conditions that generate a potential difference, for example



500 by maintaining a larger effective pressure drop, sharpening spatial ion distributions near the
501 evaporating region, and/or stabilizing wet–dry asymmetry along the device. Accordingly, the
502 measured voltage was expressed as the sum of a streaming contribution and an evaporation-
503 associated contribution:

$$V_{OC} = V_{str} + V_{evap} \quad (14)$$

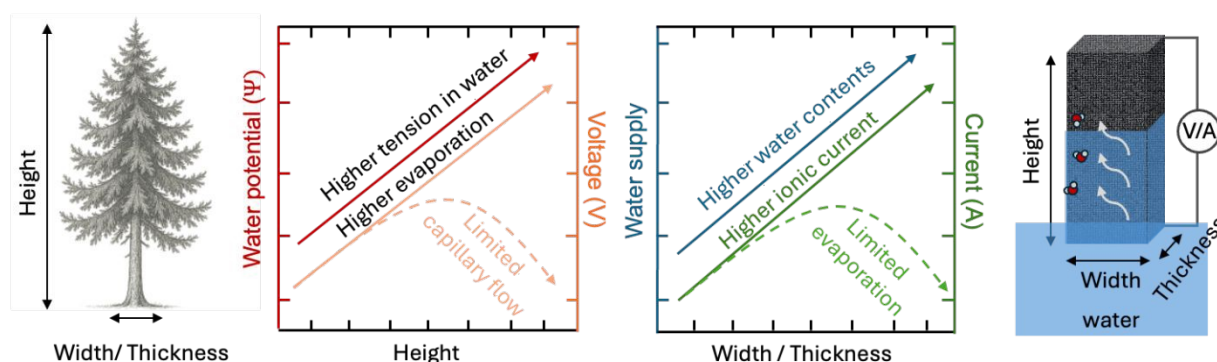
504 where V_{OC} represents the open-circuit voltage measured experimentally, V_{str} is the streaming
505 potential calculated using Equation (11), and V_{evap} denotes the additional voltage attributed to
506 evaporation. The authors further related V_{evap} to an evaporation-associated power density W by
507 invoking the latent heat of vaporization F and the mechanical work associated with liquid
508 evaporation ω :³

$$W = \frac{F\omega}{L} \quad (15)$$

509 This expression is heuristic and does not, by itself, provide a direct route to predict the
510 voltage magnitude from independently measurable transport parameters. Nevertheless, the
511 qualitative conclusion is robust: evaporation can measurably boost hydrovoltaic output. This is
512 reminiscent of transpiration in trees, where evaporation at leaves generates strongly negative water
513 potentials that both sustain and intensify long-range transport. Taken together, these observations
514 reinforce the conceptual alignment between plant hydraulics and TIH operation. Evaporation
515 sustains device function and, in some architectures, measurably enhances performance. This
516 perspective motivates the comparisons developed in the following sections, where we examine
517 how macroscopic geometry, pore-scale structure, and environmental conditions that govern
518 transpiration in trees similarly regulate output in TIH systems, and how these insights can be used
519 to improve power-generation efficiency.

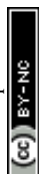
520 **5. Macroscopic Geometric Variables that Shape TIH Performance: Length, Thickness, and** 521 **Width**





522
 523 **Figure 5. Linking macroscopic substrate geometry to liquid transport in trees and TIH**
 524 **devices.** In trees (left), height sets the gravitational component of water potential and increases
 525 hydraulic resistance, requiring more negative potentials at the crown to sustain ascent. In TIH
 526 devices (right), increasing vertical length can increase cumulative evaporation and the resulting
 527 electrokinetic migration, often raising the measured voltage; however, excessive evaporative
 528 demand can outpace capillary replenishment, induce partial drying, and suppress output. In trees,
 529 trunk diameter (width) reflects both mechanical stability and hydraulic capacity. In TIH devices,
 530 width and thickness (lateral dimensions) set the number of parallel flow pathways and interfacial
 531 area available for ion transport, typically increasing current. Yet if the device becomes too thick,
 532 evaporation-driven throughflow can be hindered by longer diffusion paths and increased internal
 533 flow resistance, reducing current despite larger cross-sectional area.

534 It is estimated that ~73,000 tree species exist worldwide.⁵³ Owing to differences in genetics,
 535 climate, competition for light and space, water availability, and soil quality, trees exhibit a wide
 536 range of macroscopic geometries, most notably in height and trunk diameter.^{54–56} These geometric
 537 differences directly shape the physics of water transport. Greater height can confer improved
 538 access to sunlight and thus enhance photosynthetic potential. However, increasing height also
 539 imposes a larger gravitational head and requires the maintenance of more negative water potentials
 540 at the crown to sustain sap ascent through xylem. In general, xylem water potential decreases
 541 approximately linearly with tree height and can reach values as low as -2 MPa.⁵⁷ This trend is
 542 broadly observed across major tree groups, including both angiosperms and gymnosperms.⁵⁸
 543 Under such extreme tension, the likelihood of cavitation increases, particularly under water
 544 deficient conditions such as drought or during daytime exposure to intense sunlight and elevated
 545 temperatures. Cavitation can lead to hydraulic failure and, ultimately, mortality, thereby imposing
 546 a fundamental limit on upward growth. Furthermore, increasing tree height demands a



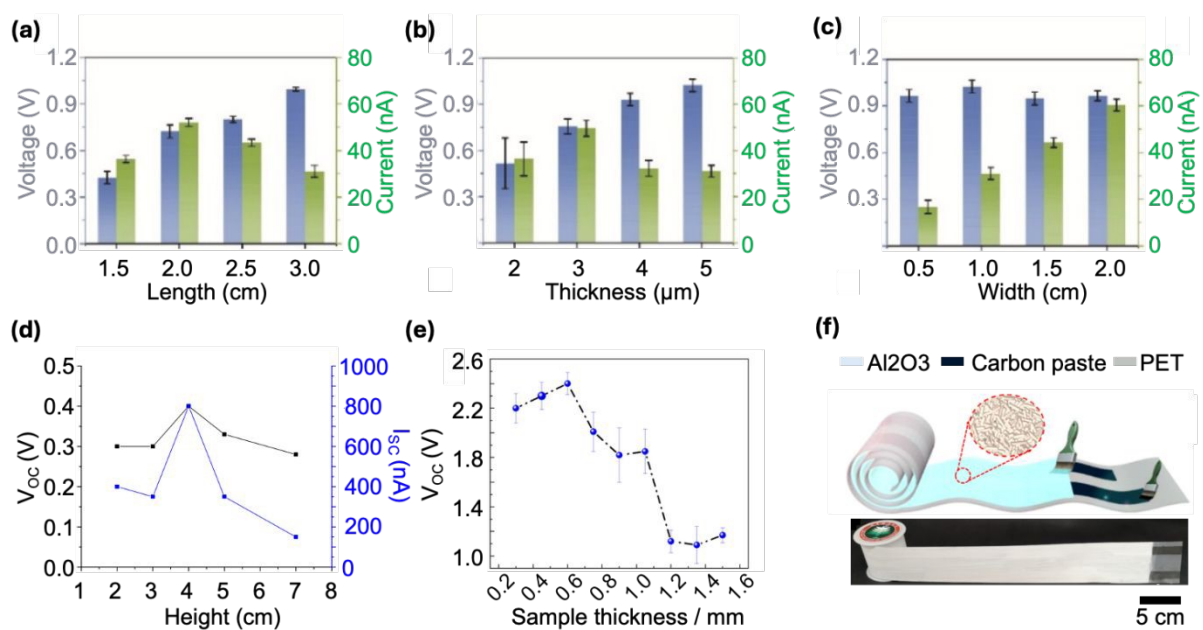
547 mechanically stronger xylem network to support trunk mass against gravity, indicating that both
548 cavitation resistance and structural stability constrain how negative xylem pressures can
549 become.^{34,59} To mitigate cavitation risk arising from highly negative water potentials and limited
550 sap availability, tall trees may reduce transpiration through stomatal closure, while hydraulic
551 resistance also naturally increases along longer xylem pathways, slowing flow and reducing the
552 rate of water loss.⁶⁰ In parallel, trees achieve mechanical stability through trunk thickening, which
553 not only provides structural reinforcement but also increases hydraulic capacitance and internal
554 water storage, thereby buffering transient imbalances between water supply and evaporative
555 demand.⁶¹

556 At the same time, water availability, water potential, and tree size significantly influence
557 rooting depth and lateral root spread.^{62,63} In water-rich environments with high precipitation, roots
558 often expand both deeper and farther laterally because water and nutrients can be accessed from
559 multiple soil layers. This favorable water supply promotes increases in both height and girth, which
560 in turn require a more extensive root network to provide greater water uptake and mechanical
561 anchoring. A larger root system also improves soil reinforcement, helping prevent uprooting under
562 gravitational and wind loading. In contrast, trees in arid climates adopt a wider range of rooting
563 strategies depending on species.⁶⁴ For example, phreatophytes develop deep roots that can access
564 groundwater, allowing them to maintain high transpiration rates. On the other hand, cacti typically
565 form shallow but laterally extensive root systems that maximize the capture of episodic surface
566 moisture, while minimizing water loss through strong suppression of leaf area. Taken together,
567 species identity, water availability, gravity, cavitation risk, and material strength collectively bound
568 attainable macroscopic size and form, confining extreme tree heights to a narrow hydraulic
569 operating envelope.

570 A closely related geometry–transport coupling appears in transpiration-inspired
571 hydrovoltaics (TIH), which can be viewed as engineered, electricity-generating analogs of trees.
572 In TIH devices, macroscopic dimensions do not simply define electrode spacing or active area;
573 they also regulate the balance among capillary replenishment, evaporative demand, and internal
574 flow resistance. Together, these factors determine the saturation profile and the interfacial
575 conditions required for electrokinetic transduction. As a result, device length often correlates with
576 voltage output, whereas width and thickness more strongly influence current by increasing the
577 number of parallel flow pathways, wetted interfacial area, and overall liquid throughput. These



578 trends, however, are not universal and may reverse depending on material properties and on
 579 whether the dominant transduction mechanism is electrokinetic streaming (for dielectric
 580 capillaries), pseudo-streaming (for electrically conductive capillaries), or ionovoltaic coupling that
 581 is often seen inside semiconducting channels.



582
 583 **Figure 6. Device dimensions, output trends, and scaling strategies guided by geometry–**
 584 **performance relationships. (a–c) Voltage and current versus length, thickness, and width for a**
 585 **vermiculite-based TIH device. Reproduced with permission. Copyright 2023, Elsevier.⁶⁵ (d, e)**
 586 **Voltage and current versus height and thickness for Al₂O₃-based device, highlighting non-**
 587 **monotonic behavior arising from the competition between evaporation rate and capillary**
 588 **replenishment. Reproduced with permission.⁴⁹ Copyright 2022, American Chemical Society. (f)**
 589 **Scaled-up TIH system on a flexible PET substrate with deposited Al₂O₃ and carbon-paste**
 590 **electrodes, demonstrating a practical route to increase current by increasing effective lateral area**
 591 **and parallel pathways. Reproduced with permission.⁶⁶ Copyright 2019, American Chemical**
 592 **Society.**

593 5.1 Effect of device length on power output

594 A frequently reported trend is that open-circuit voltage increases with device length,
 595 whereas short-circuit current exhibits a nonmonotonic (volcano-shaped) dependence on
 596 length.^{36,65,67–72} In a representative study, Li et al. printed vermiculite, a layered mineral with strong



597 ion-selective properties, onto quartz.⁶⁵ The stacked flake morphology formed parallel
598 nanochannels that supported selective cation transport. Increasing the channel length from 2 to 3
599 cm raised the open-circuit voltage from ~0.75 V to nearly 1.0 V. By contrast, the short-circuit
600 current rose from ~40 nA at 1 cm to ~50 nA at 2 cm but decreased upon further length extension
601 (Figure 6a).

602 Li et al. interpreted the output within a streaming-potential framework. The observed
603 length dependence, however, highlights a practical limitation of applying classical streaming
604 theory directly to evaporatively driven TIH devices. In the classical expression (Equation 11), V_{str}
605 depends on the driving pressure drop Δp but does not explicitly depend on channel length.
606 Moreover, for idealized channels, the streaming current can be expressed in a form proportional
607 to the pressure gradient:

$$I_{str} = \int_{-R}^R \rho_e(r) v_x(r) dr = \frac{\epsilon_r \epsilon_0 r^2 \zeta \Delta P}{\mu L} \quad (16)$$

608 where r is the pore radius and L is the channel length. If other parameters are held constant and Δ
609 P is fixed, increasing L reduces the pressure gradient $\Delta P/L$ and therefore decreases I_{str} , opposite
610 to the initial rise observed experimentally. This discrepancy suggests that under evaporative
611 operation, ΔP , saturation state, and effective transport parameters (for example, permeability,
612 conductivity, and interfacial charge regulation) are not invariant with length.

613 A useful way to reconcile these discrepancies is to treat evaporation as the missing coupling
614 between geometry and driving forces. For instance, Li et al. proposed that longer channels can
615 sustain greater cumulative evaporation, which strengthens capillary replenishment and amplifies
616 charge separation along the vermiculite surface up to an optimal length. Beyond this threshold,
617 distributed evaporation promotes partial drying and increases internal flow resistance, leading to
618 continued voltage growth but reduced current.

619 5.2 Effect of device thickness: voltage enhancement and nonmonotonic current

620 By varying the number of coating cycles, Li et al. tuned the thickness of the vermiculite
621 film. The output voltage increased with thickness, whereas the current increased to a maximum
622 and then declined (Figure 6b). The authors proposed that thicker films can sustain a larger “charge



623 imbalance,” resulting in higher voltage, but that excessive thickness increases internal flow
624 resistance and reduces evaporation, impeding ion transport and lowering current.

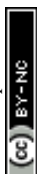
625 **5.3 Effect of device width: weak voltage dependence and increased current**

626 When Li et al. increased the film width at fixed length and thickness, the voltage remained
627 nearly constant, while the current increased approximately proportionally (**Figure 6c**). This scaling
628 is consistent with width primarily adding parallel pathways: increasing width increases cross-
629 sectional area for water and ion transport (and often the total wetted interfacial area), thereby
630 increasing current. Because width does not substantially change the longitudinal transport distance
631 between electrodes, it has a weaker effect on the axial gradient that sets the potential, and the
632 voltage can remain largely unchanged.

633 **5.4 Deviations in geometry dependence across the literature**

634 The relationship between channel length and voltage generation is not universally
635 monotonic.^{49,73–75} For example, Chaurasia et al. coated Al₂O₃ nanoparticles onto a substrate and
636 operated the HV device in deionized water.⁴⁹ Both open-circuit voltage and short-circuit current
637 increased with length up to 4 cm but declined sharply beyond that value (**Figure 6d**). The authors
638 attributed this decline to an evaporation–replenishment mismatch: beyond an optimal length,
639 evaporation depletes the capillary-supplied water film faster than it can be replenished, thinning
640 or breaking the continuous wetted pathway needed for ion transport and EDL formation near the
641 upper electrode. In this regime, both the electrokinetic driving and the effective conductivity
642 deteriorate, reducing voltage and current. Chaurasia et al. also reported a thickness dependence
643 that differed from the vermiculite system (**Figure 6e**). After an initial increase in voltage as
644 thickness increased from 0.2 to 0.6 mm, both voltage and current decreased with further thickness
645 increase. They again invoked evaporation–transport coupling, proposing that thicker Al₂O₃ layers
646 hinder evaporation and water transport, thereby weakening interfacial gradients and reducing the
647 potential difference between electrode regions.

648 Across the literature, such discrepancies are expected to be material- and morphology-
649 dependent, reflecting differences in porosity, tortuosity, wettability, surface charge regulation,
650 water retention, and the relative magnitudes of ionic and electronic conductivities. Despite these
651 variations, a consistent physical theme emerges. evaporation both drives flow and helps maintain
652 the interfacial asymmetries that enable charge separation and ion transport. Under moderate



653 conditions, stronger evaporation can enhance output. Once evaporation exceeds a critical threshold
654 relative to capillary replenishment, partial drying and increased resistance suppress transport and
655 degrade performance. At present, however, there is no quantitative framework that directly links
656 evaporation dynamics and saturation profiles to electrokinetic source terms and internal resistances,
657 and the community relies on qualitative explanations even when observed trends differ.

658 Fortunately, the role of evaporation is well understood in natural transpiration systems,
659 where it generates negative pressure to drive water transport. Taller trees require more negative
660 water potentials, but this requirement is bounded by cavitation risk and hydraulic conductivity.
661 Larger trunk diameters improve mechanical support and storage but increase the water demand
662 needed to sustain the vascular network. By benchmarking this balance between water transport
663 and structural dimensions in trees, a deeper understanding of how evaporation influences
664 electrokinetic phenomena, and how water–solid interactions vary across different materials will
665 be essential to elucidate the relationship between geometric dimensions and power output in TIH
666 devices.

667 **5.5 Coupling of geometry and interfacial electrokinetics to maximize TIH efficiency**

668 Building on these geometric effects, several studies have explored scaling strategies to
669 increase hydrovoltaic output.^{66,76–79} Shao et al. deposited Al₂O₃ nanoparticles on a flexible PET
670 substrate to fabricate a rollable TIH device (**Figure 6f**).⁶⁶ A 4 cm × 4.5 cm sample produced ~2.5
671 V and 200 nA. Increasing the device width to 18 cm increased the output current to ~800 nA,
672 demonstrating scalable current generation via lateral expansion. Although only width was varied
673 in this study, the results highlight the promise of large-area manufacturing. A more quantitative
674 understanding of evaporation-driven electrokinetics should enable predictive scaling of length and
675 thickness as well, improving both absolute output and overall energy-conversion efficiency.

676 **6. Microscopic Variables that Affect TIH Performance: Channel Conformation and** 677 **Alignment**

678 Plants sustain transpiration by integrating hierarchical xylem architectures with strong
679 directional anisotropy.^{80–82} Gymnosperms (for example, conifers and other softwoods) rely
680 primarily on tracheids, which are elongated, narrow conduits that couple water transport with
681 mechanical support. Angiosperms (hardwoods) typically exhibit more heterogeneous xylem
682 anatomy that includes vessels, fibers, and parenchyma, enabling higher hydraulic conductivity but

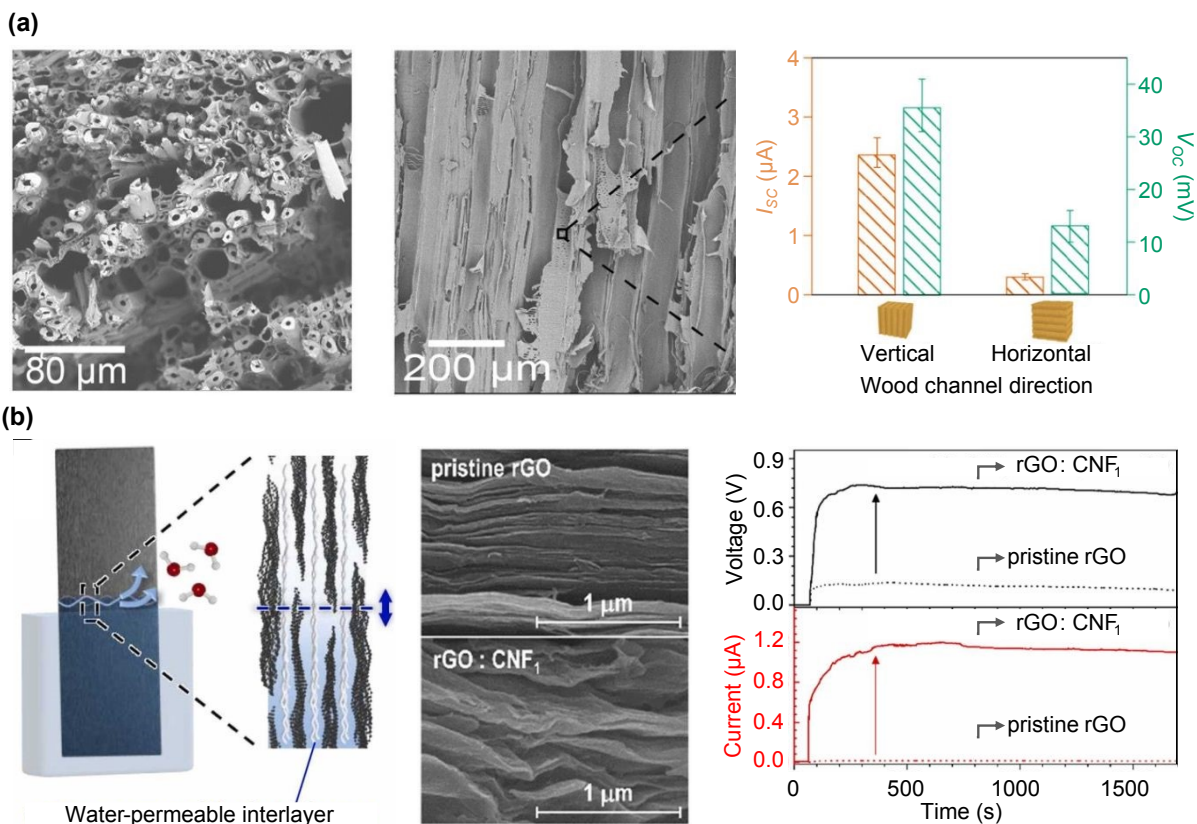


683 also introducing additional pathways for storage and regulation.^{83,84} Even within a single tree,
684 conduit diameter is not uniform. Xylem elements are generally wider near the base, where lower
685 tension is required to sustain flow, and become narrower toward the crown, where water must be
686 transported under more negative pressures and the risk of embolism increases. Narrower conduits
687 at height reduce vulnerability to cavitation and help preserve hydraulic continuity, even at the cost
688 of higher flow resistance.⁸⁵ Beyond channel diameter, plants employ structural motifs that localize
689 and compartmentalize flow. Scalariform perforation plates and related pit structures subdivide
690 pathways and distribute resistance, helping to limit the spread of cavitation events and maintain
691 transport through parallel routes.⁸⁶ In this sense, plant xylem is not optimized solely for low
692 resistance; it is optimized for sustained function under fluctuating evaporative demand, balancing
693 throughput, safety from embolism, and spatial control of water–air interfaces.

694 Because TIH devices generate electricity by coupling evaporation-sustained capillary flow
695 coupled to interfacial electrokinetics, channel architecture is a primary design variable. Pore
696 conformation and alignment regulate (1) hydraulic conductance and the ability to sustain
697 directional flow, (2) the extent and location of the water–air interface that sets the evaporation
698 boundary condition, and (3) the degree of ionic selectivity and EDL overlap under confinement.
699 In this section, we survey the most common microstructural motifs in TIH, including vertically
700 aligned, parallel, honeycomb, random, and hierarchical architectures. For each, we summarize the
701 reported advantages and then highlight the unresolved question that recurs across the literature:
702 how to quantitatively connect geometry to evaporation kinetics, ion selectivity, and electrical
703 output under controlled comparisons.

704





705

706 **Figure 7. Vertical and parallel Align Channel conformations used in TIH devices and**707 **representative output characteristics. (a)** Vertically aligned channels templated by natural wood.

708 SEM images show top and side views of preserved xylem clusters; the plot compares

709 voltage/current for devices oriented with channels vertical versus horizontal. Reproduced with

710 permission.⁸⁷ Copyright 2020, American Chemical Society. **(b)** Parallel nanochannels in an711 rGO:CNF₁ composite film. The interlayer gap is larger than in pristine rGO, facilitating water712 transport; plots compare voltage/current of rGO:CNF₁ (solid) and rGO (dashed). Reproduced with713 permission.⁸⁸ Copyright 2024, Elsevier.

714

715 **6.1 Vertically aligned channels inspired by plant vasculature**

716 Vertically aligned microchannels are the most direct synthetic analogue of plant

717 vasculature and have been widely explored in TIH devices.^{87,89–91} One common strategy is to use

718 natural wood as a template. Zhou et al. chemically modified beech wood with citric acid to

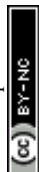
719 introduce carboxyl and hydroxyl groups and increase the negative surface charge.⁸⁷ Carbon-paste

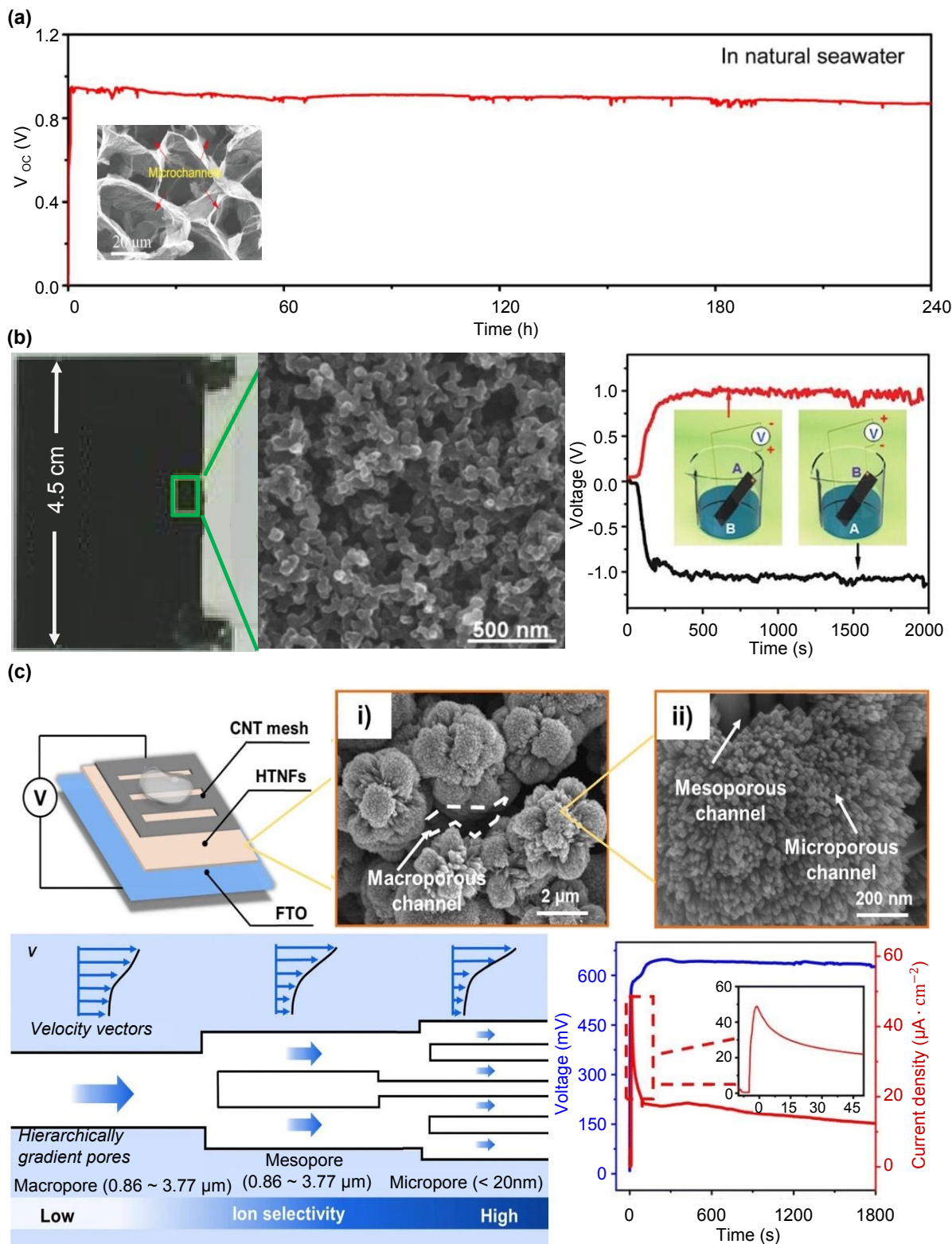
720 electrodes supported on a PET mesh were attached to the top and bottom surfaces. When the
721 bottom of the wood block was immersed in deionized water, capillary transport occurred through
722 preserved xylem channels and evaporation proceeded from the exposed top surface. Proton
723 dissociation from carboxyl groups established EDLs, and the device produced ~ 30 mV and ~ 2 μ A,
724 which the authors interpreted using a streaming-potential mechanism (**Figure 7a**). The intrinsic
725 anisotropy of wood provides a clear test of the role of alignment. Rotating the block by 90°
726 reoriented the dominant channels from vertical to horizontal, suppressing transport toward the top
727 electrode and reducing output (voltage to ~ 15 mV and current to below 1 μ A). This comparison
728 supports a general design principle: directional, aligned pathways increase hydraulic conductance
729 and maintain a stable saturation gradient, which strengthens sustained ion transport and therefore
730 electrical output.

731 A practical limitation of many vertically aligned systems is the evaporation boundary
732 condition: if only a small outlet region is exposed, the effective water–air interfacial area is
733 restricted. Some studies have therefore introduced solar irradiation or localized heating to
734 accelerate evaporation. While these approaches can increase output, they complicate deployment
735 by relying on external energy input and by coupling device performance to illumination or heating
736 conditions rather than to intrinsic structural design.

737 **6.2 Parallel nanochannels in two-dimensional materials**

738 Parallel nanochannels assembled from two-dimensional (2D) materials provide an
739 alternative route to strong confinement with high interfacial area.^{65,72,79,88,92} Layered materials
740 naturally form slit-like channels upon stacking, and their large specific surface area can enhance
741 ion–surface interactions that govern EDL formation and selective transport. Yu et al. fabricated a
742 composite of reduced graphene oxide (rGO) and cellulose nanofibers in which rGO nanosheets
743 assembled into a largely parallel, layered architecture (**Figure 7b**).⁷² This alignment created
744 extended nanochannels with high surface area and promoted strong ion–channel coupling. When
745 tested in deionized water, the device generated an open-circuit voltage exceeding 0.6 V and a short-
746 circuit current of approximately 1 μ A. These results illustrate the appeal of 2D assemblies: channel
747 alignment and surface area are built into the material platform, enabling high output in compact
748 geometries.





749

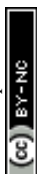
750 **Figure 8. Micro-, Nano-, and Hierarchically structured channel conformations used in TIH**751 **devices and representative output characteristics. (a) Honeycomb rGO formed by freeze-**

752 casting/freeze-drying. The cellular structure increases interfacial area and supports stable operation
753 in saline water; the plot shows long-term voltage stability in natural seawater. Reproduced with
754 permission.⁹³ Copyright 2021, American Chemical Society. **(b)** Random porous network formed
755 from amorphous carbon-black nanoparticles collected from toluene soot. The left panel shows a
756 photograph of the device (channel length ~ 4.5 cm). The middle panel is an SEM image
757 highlighting the disordered porous microstructure. The right panel shows the voltage output;
758 reversing the electrode connections flips the voltage polarity while leaving the magnitude nearly
759 unchanged, consistent with an interfacial origin of the signal. Reproduced with permission.⁹⁴
760 Copyright 2017, John Wiley VCH. **(c)** Hierarchical device comprising 3D dendritic TiO₂
761 nanoflowers, a CNT mesh, and FTO electrodes. The top-left panel illustrates the device concept.
762 The top-middle and top-right SEM images show TiO₂ nanoflowers grown on FTO and the
763 resulting multiscale pore network. The bottom-left schematic summarizes the hierarchical channel
764 architecture from macro- to micropores; the blue arrow indicates the water-flow direction,
765 emphasizing high permeability in macropores coupled with enhanced ion selectivity in micropores.
766 The bottom-right panel reports the voltage and current-density response upon droplet addition
767 (inset: enlarged view of the initial current peak). Reproduced with permission.⁷⁵ Copyright 2024,
768 The Royal Society of Chemistry.

769

770 **6.3 Honeycomb architectures that couple evaporation area with salt tolerance**

771 Honeycomb-like porous microstructures provide large interfacial area and distributed
772 pathways that can simultaneously enhance evaporation and mitigate fouling.^{93,95} Wu et al. formed
773 a porous rGO honeycomb by casting an rGO suspension on a cold substrate, where ice-crystal
774 templating generated a cellular network that was retained after freeze-drying (**Figure 8a**).⁹³ The
775 device operated in NaCl-containing reservoirs and produced an open-circuit voltage above 0.8 V
776 in natural seawater, maintaining output for over 240 hours. A notable advantage was resistance to
777 salt crystallization: the honeycomb geometry suppressed salt accumulation during prolonged
778 saline operation, whereas a control sample cast on a warm substrate formed dense rGO layers,
779 showed substantially lower voltage, and rapidly decayed to ~ 0 V as salt crystals formed, blocked
780 transport, and disrupted interfacial charge separation. These results emphasize that channel
781 confirmation should be evaluated not only by peak output, but also by operational stability. Under



782 high salinity, maintaining open flow paths and avoiding crystallization at evaporative fronts is
783 critical. Honeycomb microstructures offer a promising route because they distribute evaporation
784 over many pores, reduce local supersaturation hotspots, and provide parallel transport routes that
785 remain functional even if a fraction of pathways partially foul.

786 **6.4 Random porous networks and ion selectivity through EDL overlap**

787 Most TIH devices reported to date employ random porous networks created by packing
788 nanoparticles without long-range alignment.^{36,42,43,49,66–68,70,71,73,74,77,94,96–112} These structures are
789 straightforward to fabricate and can deliver high output because they provide large interfacial area
790 and nanoscale confinement. Ding et al. printed a toluene-soot slurry on an Al₂O₃ substrate to form
791 a disordered carbon-black network with pore sizes spanning tens to hundreds of nanometers
792 (**Figure 8b**).⁹⁴ The negatively charged soot attracted cations from deionized water, promoting EDL
793 formation. Importantly, under low ionic strength, a subset of pores can approach the Debye length,
794 enabling EDL overlap that enhances selectivity by enriching counterions and excluding co-ions.
795 The device generated an open-circuit voltage of approximately 1.0 V in deionized water. Random
796 networks therefore illustrate a recurring trade-off in TIH: tortuosity and narrow constrictions can
797 enhance selectivity and interfacial polarization, but they also increase hydraulic resistance and can
798 make operation more sensitive to drying, fouling, and changes in electrolyte conductivity.

799 **6.5 Hierarchical micro–nano structures that balance ion conductance and selectivity**

800 Hierarchical architectures aim to combine the advantages of fast transport in larger pores
801 with strong selectivity in smaller pores.^{75,113} Wang et al. proposed that macropores (micrometer-
802 scale) provide low hydraulic resistance and rapid imbibition, whereas mesopores and micropores
803 (tens of nanometers and below) promote ion selectivity through EDL overlap (**Figure 8c**).⁷⁵ In
804 their implementation, three-dimensional hierarchically structured TiO₂ nanoflowers were grown
805 on FTO substrates by hydrothermal synthesis, with a CNT mesh used as the top electrode.
806 Electricity generation was probed by depositing a water droplet on the structure. By tuning
807 precursor and HCl concentrations, the authors adjusted the pore-size distribution and observed
808 corresponding changes in voltage and current. The design goal is explicit: couple efficient water
809 transpiration flux with selective interfacial ion transport within a single, multiscale architecture.

810 **6.6 Toward controlled structure–function maps for TIH microarchitecture**



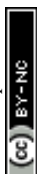
811 Despite the diversity of channel conformations reported, there has been little systematic
812 effort to compare architectures under controlled conditions. In many studies, changes in
813 microstructure are accompanied by simultaneous changes in chemistry, surface charge,
814 conductivity, or mechanical properties, making it difficult to isolate geometric effects. As a result,
815 even for fixed active material loading and comparable pore volume or surface area, there is no
816 consensus to a basic design question: which channel geometry (vertically aligned, parallel layered,
817 honeycomb, random, or hierarchical) is optimal for a given operating condition, such as across
818 water sources spanning wide salinity ranges?

819 Addressing this gap will require targeted studies that decouple channel geometry,
820 confirmation from material composition, and salinity effects across different TIH platforms. One
821 practical approach is to fabricate families of architectures from the same material platform (or with
822 matched surface chemistry) while independently measuring hydraulic conductance, evaporation
823 flux, saturation profiles, and effective ionic selectivity. Linking these measurements to electrical
824 output would enable structure–function maps that clarify how channel conformation controls (1)
825 water transport and replenishment, (2) spatial localization of evaporation, (3) EDL overlap and ion
826 selectivity, and (4) internal electrical resistance. Such controlled comparisons would move TIH
827 channel design from qualitative analogy to predictive engineering, enabling architectures that are
828 optimized not only for peak output but also for stability under real-world conditions.

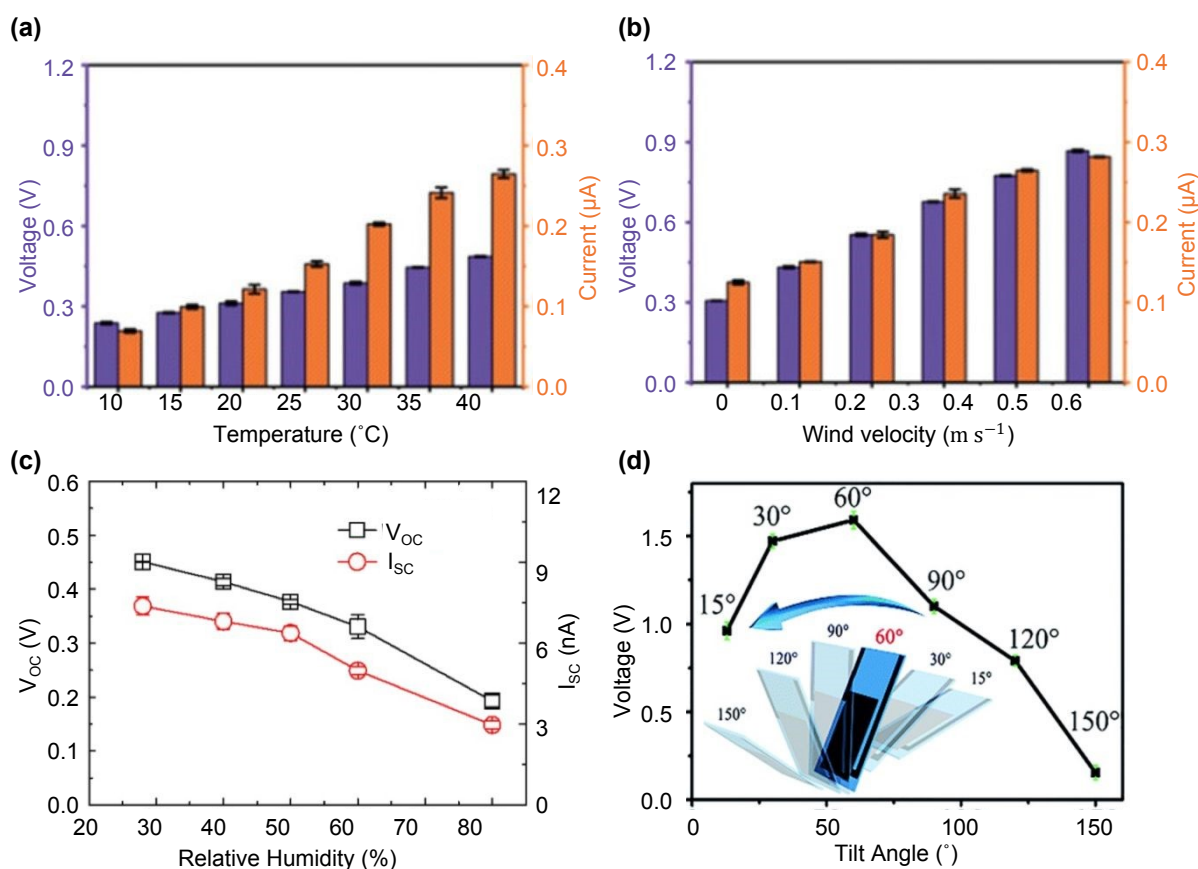
829

830 **7. Environmental Variables that Affect TIH Performance: Temperature, Humidity, Airflow,** 831 **and Salinity**

832 Plant transpiration is strongly regulated by the environment.^{55,114,115} Temperature, relative
833 humidity, and solar irradiation set the evaporative demand at the leaf surface, while airflow
834 controls convective mass transfer and therefore the evaporation flux. Because TIH devices rely on
835 the same evaporation-sustained capillary transport to maintain interfacial ion redistribution and
836 electrical output, these environmental variables become intrinsic “operating conditions” rather
837 than external perturbations. Consistent with this coupling, many studies report pronounced
838 changes in voltage and current when temperature, humidity, and airflow are varied, and when the
839 device is reoriented relative to gravity and the surrounding air.¹¹⁶



840 In this section, we summarize the dominant environmental parameters that shape TIH
 841 performance: ambient temperature, airflow velocity, relative humidity, and device orientation. We
 842 also distinguish between continuous-flow TIH systems, where evaporation amplifies both the
 843 driving force and the electrokinetic response, and droplet-driven or pseudo-streaming systems,
 844 where evaporation primarily sets the operational lifetime rather than the output amplitude. We
 845 conclude with emerging strategies for environmentally robust architectures that maintain stable
 846 output despite ambient fluctuations.



847
 848 **Figure 9. Environmental control of TIH output through evaporation rate. (a, b)** Voltage and
 849 current versus temperature and wind velocity. Higher temperature and airflow increase evaporative
 850 demand and typically amplify both voltage and current. Reproduced with permission.⁶⁷ Copyright
 851 2022, Wiley VCH. **(c)** Voltage and current decrease with increasing relative humidity, consistent
 852 with suppressed evaporation. Reproduced with permission.⁴³ Copyright 2019, American Chemical
 853 Society. **(d)** Voltage versus device tilt angle (15–150 $^{\circ}$), reflecting the balance between evaporation



854 flux and capillary supply under gravity. Reproduced with permission.⁹⁶ Copyright 2019, Royal
855 Society of Chemistry.

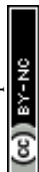
856

857 **7.1 Temperature and airflow increase TIH output by increasing evaporative demand**

858 Several studies that have systematically examined temperature and wind effects report that
859 both open-circuit voltage and short-circuit current increase with elevated evaporative
860 demand.^{67,77,93,106,111,117–119} Chi et al. tested a porous, hydrophilic Al₂O₃-based HV device with top
861 and bottom electrodes inside a programmable chamber that enabled independent control of
862 temperature and relative humidity.⁶⁷ Under fixed humidity, increasing temperature increased both
863 voltage and current (**Figure 9a**). The authors attributed this enhancement to accelerated
864 evaporation, which increases capillary replenishment and strengthens the pressure and
865 concentration gradients that drive ion transport through the micro–nanoporous network. Airflow
866 produces a closely related effect. Increasing wind speed across the device surface increased both
867 voltage and current (**Figure 9b**), consistent with convective mass transfer: faster airflow reduces
868 the boundary-layer thickness, increases the evaporation flux, and therefore increases the capillary
869 flow rate needed to replenish liquid lost at the evaporating interface. In TIH devices where
870 electrical output scales with sustained liquid or ionic transport, increased evaporation therefore
871 amplifies both voltage and current.

872 **7.2 Relative humidity suppresses evaporation and reduces TIH output**

873 Relative humidity (RH) directly controls the vapor-pressure driving force for evaporation
874 and is therefore among the most influential ambient parameters for TIH performance. Multiple
875 reports show that sealing a TIH device, which drives the local RH toward saturation, rapidly
876 eliminates the voltage signal, indicating that evaporation is required not only to initiate but also to
877 sustain electricity generation.^{43,65,67,92,106,117,120} Quantitative RH dependence has also been
878 demonstrated. Yoon et al. fabricated a nanoporous ZnO film on an Al₂O₃ ceramic substrate and
879 measured output as RH was varied under otherwise comparable conditions. Both open-circuit
880 voltage and short-circuit current decreased strongly with increasing humidity (**Figure 9c**). For
881 example, the voltage dropped from ~0.45 V at 30% RH to ~0.2 V at 80% RH, while the current
882 decreased from ~7 nA to ~3 nA over the same range. These results are consistent with suppressed



883 evaporation at high RH, which reduces capillary-driven replenishment and weakens the sustained
884 ion redistribution required for EDL-mediated transduction.

885 **7.3 Device orientation tunes the balance between capillary supply, gravity, and evaporation**

886 The inclination angle of a TIH device can significantly affect output by changing the
887 competition between capillary transport, gravitational drainage, and access of the active surface to
888 air. Liu et al. deposited a composite film of carbon nanospheres and TiO₂ nanowires on glass,
889 integrated a CNT electrode, and operated the device with the bottom electrode submerged in
890 water.⁹⁶ By varying the inclination angle from 15° to 150°, they observed a pronounced angle
891 dependence in open-circuit voltage (**Figure 9d**). At low angles, capillary transport can readily
892 drive water upward, but the evaporation boundary condition and air access may be suboptimal,
893 limiting output. As the angle increased, voltage rose and reached a maximum (reported above 1.5
894 V) near 60°, consistent with an orientation that balances continuous liquid supply with efficient
895 evaporation from the exposed surface. When the angle exceeded 90° and the active film faced
896 downward toward the water, evaporation was strongly suppressed and the voltage decreased. This
897 study highlights orientation as a practical design variable for field deployment. Because
898 evaporation is also enhanced by convection, the optimal orientation may depend not only on
899 gravity but also on airflow direction and local wind conditions.

900 **7.4 Effect of Salinity in soil water on tree metabolism**

901 Soil contains not only water but also a variety of dissolved ionic species such as Ca²⁺, Na⁺,
902 and Cl⁻. Because soil water content is highly sensitive to precipitation, season, and atmospheric
903 temperature, the salinity of water taken up by can fluctuate substantially. For example, during
904 drought, elevated soil salinity can disrupt cellular osmotic balance and impair plant metabolism,
905 ultimately reducing growth.^{121,122} This phenomena is referred to as *salinity stress*. When salinity
906 stress becomes severe, plant metabolism may collapse, leading to death. Consequently, plants have
907 evolved strategies to regulate the salinity of the sap they transport internally.

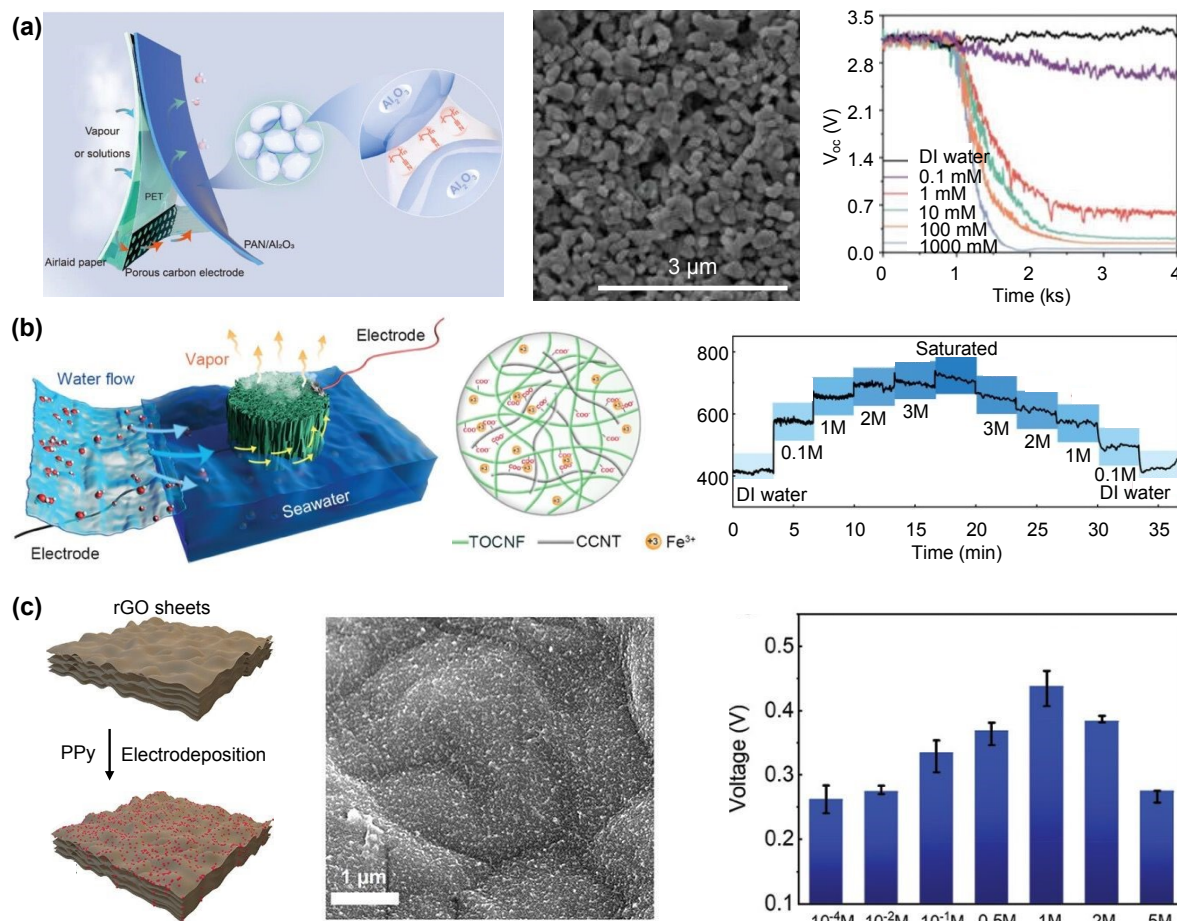
908 Notably, some species, such as mangroves, thrive in coastal environments where salinity
909 levels would be lethal to most plants by developing **microscopic filtration systems** that exclude
910 excess ions. In mangrove roots, barriers such as suberin layers and the Casparian strip restrict the
911 influx of excess ions and water.¹²³ These barriers regulate ion exchange primarily through their
912 hydrophobic surface property. This lignin-rich, waxy layer effectively blocks the passive



913 apoplastic water infiltration, forcing water and dissolved solutes to detour through the cytoplasm
914 of specialized transport cells, where ion uptake can be selectively regulated. As a result, salts can
915 enter only through controlled biological pathways. In this sense, salinity strongly influences plant
916 survival, and the plants have evolved defense mechanisms to protect themselves from fluctuations
917 in the salinity of the water they absorb.

918 Because power generation in TIH originates from electrokinetic phenomena involving
919 interactions between charged solid surface and ionic species in the electrolyte, TIH devices also
920 exhibit salinity-sensitive responses. Microscopic interactions between ions and
921 micro/nanostructured materials, together with the associated electrokinetic effects, are widely
922 considered to underlie this salinity dependence. In this section, we discuss how TIH power output
923 changes with electrolyte salinity and summarize the physical explanations currently proposed in
924 the literature. In general, the relationship between device performance and salinity follows one of
925 three scenarios: (1) voltage decreases while current increases with salt concentration; (2) both
926 voltage and current increase with salt concentration; and (3) an optimal salt concentration exists,
927 beyond which performance declines.





928

929 **Figure 10. Effect of salinity on voltage output in TIH device. (a)** Voltage decreases with
 930 increasing salinity in a PAN/Al₂O₃ nanoparticle composite TIH device. Left: schematic illustration
 931 of the device. Middle: SEM image of the PAN/Al₂O₃ film deposited on the device. Right: voltage
 932 output at different electrolyte salinities. Reproduced with permission.¹⁰³ Copyright 2023, Wiley
 933 VCH. **(b)** Voltage profile of a TIH device made of a nanocellulose-based aerogel. Left: schematic
 934 illustration of the working mechanism and crosslinked structure of the aerogel and CCNTs. Right:
 935 linear response of voltage to electrolyte concentration change. Reproduced with permission.⁷⁶
 936 Copyright 2024, Wiley VCH. **(c)** Optimal salinity for maximizing voltage output in an rGO/PPy
 937 composite TIH device. Left: schematic illustration of the device fabrication process. Middle: SEM
 938 image of PPy deposited on rGO sheets. Right: voltage profile as a function of electrolyte salinity
 939 (NaCl). Reproduced with permission.¹⁰⁷ Copyright 2023, Taylor & Francis.

940

941



942 7.4.1 Scenario (1): Voltage is inversely proportional to the salinity

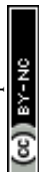
943 Several TIH devices operate through the streaming potential mechanism, which predicts a
944 decrease in voltage with increasing salinity, as discussed in Section 4.1(b). This prediction has
945 been experimentally confirmed in multiple studies.^{36,75,87,94,103} For example, Li et al. reported
946 salinity-dependent behavior consistent with the electrokinetic streaming mechanism using a device
947 composed of a PAN/Al₂O₃ composite and carbon electrodes (**Figure 10a**). In deionized water, the
948 device generated approximately 3.0 V.¹⁰³ However, as NaCl concentration increased from 0.1 to
949 1000 mM, the voltage decreased exponentially, whereas the current showed the opposite trend.
950 The decrease in streaming potential at higher salinity was attributed to compression of the EDL,
951 as described by the Debye–Hückel relation in Equation (17):

$$\lambda_D = \sqrt{\frac{\varepsilon\varepsilon_0RT}{2n_{bulk}z^2F^2}} \quad (17)$$

952
953 where λ_D is the Debye length, ε , and ε_0 are the permittivities of water and vacuum, respectively;
954 R is ideal gas constant; T is temperature; n_{bulk} is the bulk ion concentration; z is ionic valence;
955 and F is the Faraday constant. This relation indicates that increasing electrolyte concentration
956 (n_{bulk}) decreases the Debye length, thereby compressing the EDL. According to Li et al., the
957 densely packed PAN/Al₂O₃ particles are separated by gaps on the order of tens of nanometers.
958 Under deionized or sufficiently dilute conditions, λ_D can approach ~100 nm, allowing EDLs on
959 neighboring particle surfaces to overlap. Such overlap promotes ion-selective transport through
960 the channel, amplifying the ionic imbalance generated by pressure-driven flow and resulting in
961 high voltage output. As the electrolyte concentration increases, however, the EDL shrinks to only
962 a few nanometers, weakening ion selectivity and reducing the generated voltage. On the other hand,
963 the larger number of charge carriers at higher salinity increases ionic conduction and thus the
964 streaming current.

965 7.4.2 Scenario (2): Voltage is proportional to the salinity

966 In contrast to the systems described above, some TIH devices exhibit enhanced voltage
967 output in at higher salinity.^{72,76,77,124} For example, Cao et al. synthesized a nanocellulose-based



968 aerogel composite coated with the carboxylated carbon nanotubes (CCNTs) and containing
969 vertically aligned water transport channels (**Figure 10b**). While the device generates $\sim 400\text{mV}$ in
970 DI water, increasing the NaCl concentration up to near saturation point produced a monotonic
971 increase in voltage. The authors attributed this trend to a significant increase in surface charge
972 density on the channel walls. Several studies reporting similar salinity-dependent enhancement
973 have likewise suggested that higher ionic concentrations promote adsorption of more ions onto
974 channel surfaces, thereby increasing capacitive voltage generation (V_{EDL}), as discussed in Section
975 4.1(c) and equation (12). At the same time, these studies also acknowledge the streaming potential
976 mechanism, which would predict lower voltage at higher salt concentration. This apparent
977 contradiction suggests that the interplay between salinity-dependent surface charging and
978 electrokinetic transport remains insufficiently understood. In particular, the extent to which
979 enhanced surface charge density can offset EDL compression requires more rigorous theoretical
980 and experimental examination.

981 **7.4.3 Scenario (3): Optimal salinity for maximum power output**

982 Other studies have reported the existence of an optimal electrolyte salinity that maximizes
983 TIH power generation, which has been attributed to a tradeoff between enhanced surface charge
984 density and physical clogging of channel by salt crystallization during evaporation.^{93,107,125–127} For
985 example, Tian et al. observed this behavior in an rGO/polypyrrole (PPy) composite device by
986 varying NaCl concentration from 0.1 mM to 5M (**Figure 10c**). The voltage increased to $\sim 0.45\text{V}$
987 at 1M NaCl and then declined in higher concentrations. The authors proposed that the initial
988 voltage increase arose from greater ion adsorption onto the rGO/PPy surface, which increased
989 surface charge density. At higher salinity, however, rapid evaporation caused the electrolyte to
990 reach saturation more quickly, leading to salt precipitation within the pores. These precipitated
991 salts partially blocked the transport channels, reducing overall evaporation rate and offsetting the
992 benefit of increased surface charge. Although this explanation is intuitively plausible, the
993 quantitative relationship among salinity, evaporation kinetics, crystallization, and electrokinetic
994 output remains insufficiently resolved.

995 **7.4.4 Challenges in elucidating salinity dependence**

996 As discussed above, the salinity dependence of TIH power output varies substantially
997 across systems. However, a unified theoretical framework capable of explaining these different



998 trends is still lacking. For example, although some devices follow predictions from the classical
999 streaming potential mechanism, it remains unclear why these systems do not also benefit from the
1000 higher surface charge density that may arise at elevated ionic strength. Conversely, in systems that
1001 perform better at high salinity, the conditions that ultimately limit output remain poorly defined.
1002 Some devices show nearly linear performance increases up to saturation, whereas others
1003 deteriorate at much lower concentrations. Beyond qualitative hypotheses involving salt
1004 crystallization and evaporation kinetics, a more quantitative physicochemical understanding is
1005 needed. From a biological perspective, trees have evolved strategies to tolerate diverse
1006 combinations of water availability and salinity. Analogously, TIH materials may benefit from
1007 microscopic engineering approaches that enable efficient ionic transport under saline conditions.
1008 For example, incorporating ion-selective membranes or root-inspired barriers that mimic suberin-
1009 rich transport regulation may provide a route toward devices that maintain performance across a
1010 wider salinity range.

1011 **7.5 Environmentally robust architectures for persistent, stable TIH power generation**



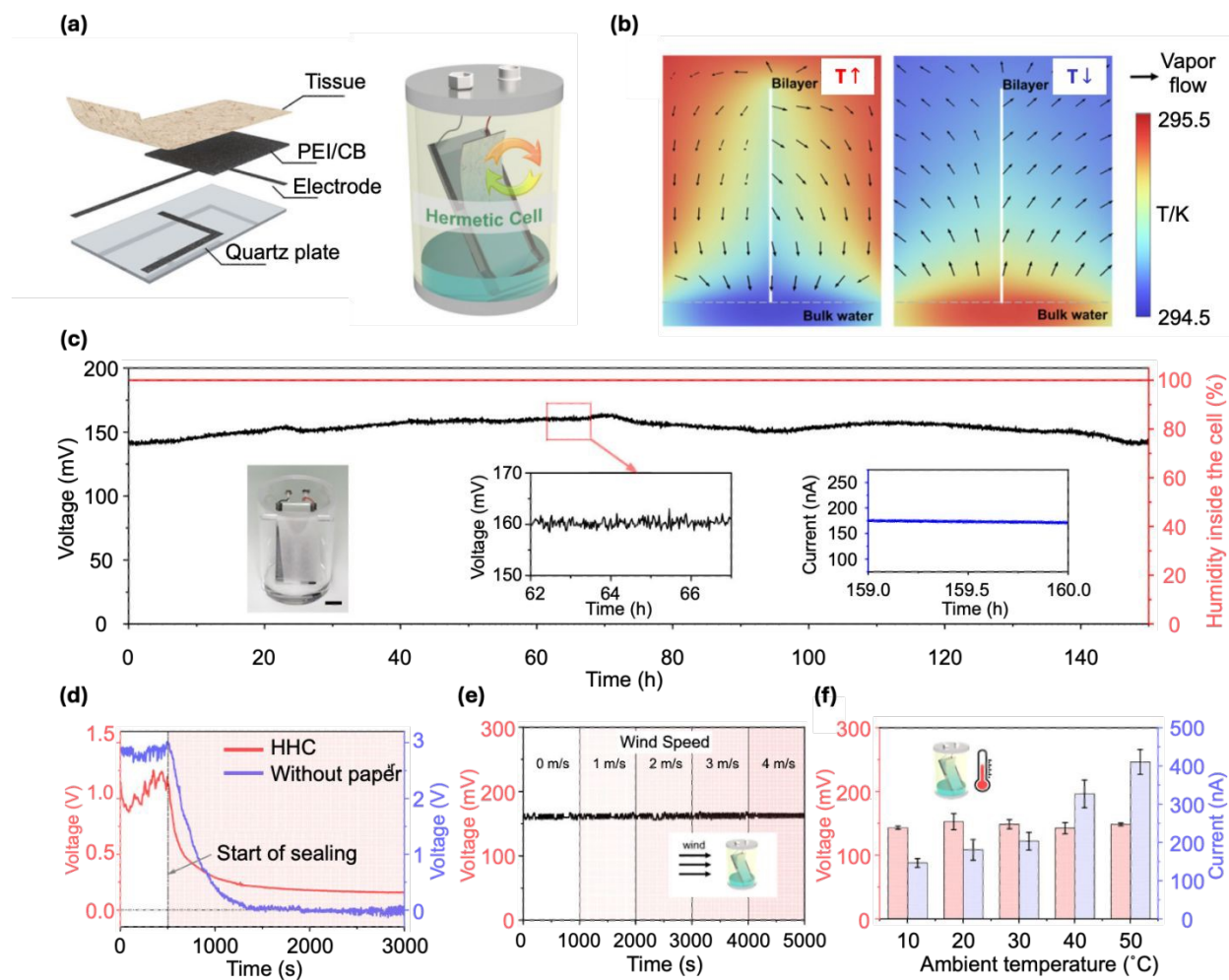


Figure 11. Self-circulating, sealed architectures for environment-insensitive power generation. (a) Hermetic-cell concept with internal liquid–vapor circulation supported by a hydrophilic tissue layer. (b) COMSOL simulations of temperature distribution and vapor flow under high- and low-ambient-temperature conditions, showing sustained internal circulation driven by an internal temperature gradient. (c) Long-term voltage/current stability in the sealed cell at internal RH \approx 100%. (d) Comparison with and without the tissue layer: the tissue maintains output after sealing, whereas output collapses without it. (e) Voltage invariance with external wind speed. (f) Voltage stability and increasing current with increasing temperature. Reproduced with permission.¹⁰⁹ Copyright 2024, Springer Nature.

The strong TIH environmental sensitivity described above can limit practical deployment, as temperature, humidity, and wind vary with weather, location, and season. To address this



1012

1013

1014

1015

1016

1017

1018

1019

1020

1021

1022

1023

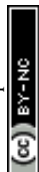
1024

1025 challenge, Yuan et al. reported a sealed HV system designed to produce stable voltage output while
1026 isolating the device from ambient fluctuations (**Figure 11a**).¹⁰⁹ In their design, carbon soot
1027 deposited on glass served as the active material and CNTs served as electrodes. The device was
1028 enclosed in a transparent cylindrical container. To prevent full saturation of the carbon film in the
1029 sealed environment, the authors introduced a highly hydrophilic paper layer that redistributed
1030 water and maintained a persistent moisture gradient between the submerged bottom region and the
1031 drier upper region. This carbon–paper bilayer functioned as a passive capillary pump. The authors
1032 proposed that the bilayer enabled a self-sustaining internal water cycle driven by minute
1033 temperature differences (reported below 1 K) (**Figure 11b**), producing internal transpiration and
1034 vapor convection that maintained operation for more than five days (**Figure 11c**). In sealed
1035 conditions, devices without the hydrophilic paper layer lost output, whereas the bilayer devices
1036 maintained voltage, underscoring the role of engineered water redistribution in sustaining the
1037 necessary spatial hydration gradients (**Figure 11d**). Airflow had little effect on voltage in the
1038 sealed configuration, consistent with isolation from external convection (**Figure 11e**), and internal
1039 humidity remained near saturation, further decoupling the system from ambient RH fluctuations.
1040 When the system temperature increased from 10 °C to 50 °C, open-circuit voltage remained nearly
1041 constant while the short-circuit current increased (**Figure 11f**). The authors attributed the stable
1042 voltage to the persistence of the moisture gradient maintained by the highly hydrophilic paper layer,
1043 while the increased current was attributed to enhanced evaporation–condensation cycling and
1044 higher ion mobility at elevated temperature.

1045 Overall, temperature, humidity, airflow, and salinity can substantially reshape TIH output
1046 because they directly regulate evaporation, capillary replenishment, and the persistence of
1047 interfacial gradients. Achieving reliable power generation therefore requires either (1) operating-
1048 condition-aware design, where geometry and deployment orientation are optimized for the local
1049 environment, or (2) self-regulating architectures, including sealed or semi-sealed systems, that
1050 maintain controlled internal water cycling and moisture gradients.

1051 8. Substrate Electrical Conductivity and TIH Device Performance

1052 As discussed in Section 4, classical streaming-potential theory is formulated for electrically
1053 insulating (dielectric) channels and typically requires Faradaic reactions at the electrodes to
1054 continuously convert an ionic streaming current into an electronic current. In contrast, pseudo-



1055 streaming and related “conductive channel” models replace the dielectric capillary wall with an
1056 electronically conductive substrate. In this setting, the solid provides an internal electronic
1057 pathway that can couple to ion motion in the liquid, allowing sustained current without relying on
1058 deliberate redox couples at the electrodes. Consequently, introducing and tuning electrical
1059 conductivity is a common design strategy in TIH devices, and varying conductive loading (or
1060 adding conductive additives) provides a straightforward knob for increasing output current.

1061 A recurring observation, however, is that electrical conductivity introduces a trade-off
1062 between open-circuit voltage and short-circuit current.^{42,50,52,110} Increasing conductivity generally
1063 increases current by reducing internal resistance, but can decrease voltage by enabling greater
1064 internal charge leakage and shunt pathways. Conversely, lower conductivity can preserve a larger
1065 voltage but limits current delivery to an external load. Many reports therefore point to an optimal
1066 conductivity, especially in composite systems, where the best performance emerges from
1067 balancing electronic conduction, capillary transport, and interfacial electrokinetic strength rather
1068 than maximizing conductivity alone.^{71–73,77,79,95,101,105,108,127,128} In this section, we summarize
1069 representative experiments and models that clarify how conductivity controls voltage, current, and
1070 overall power output.



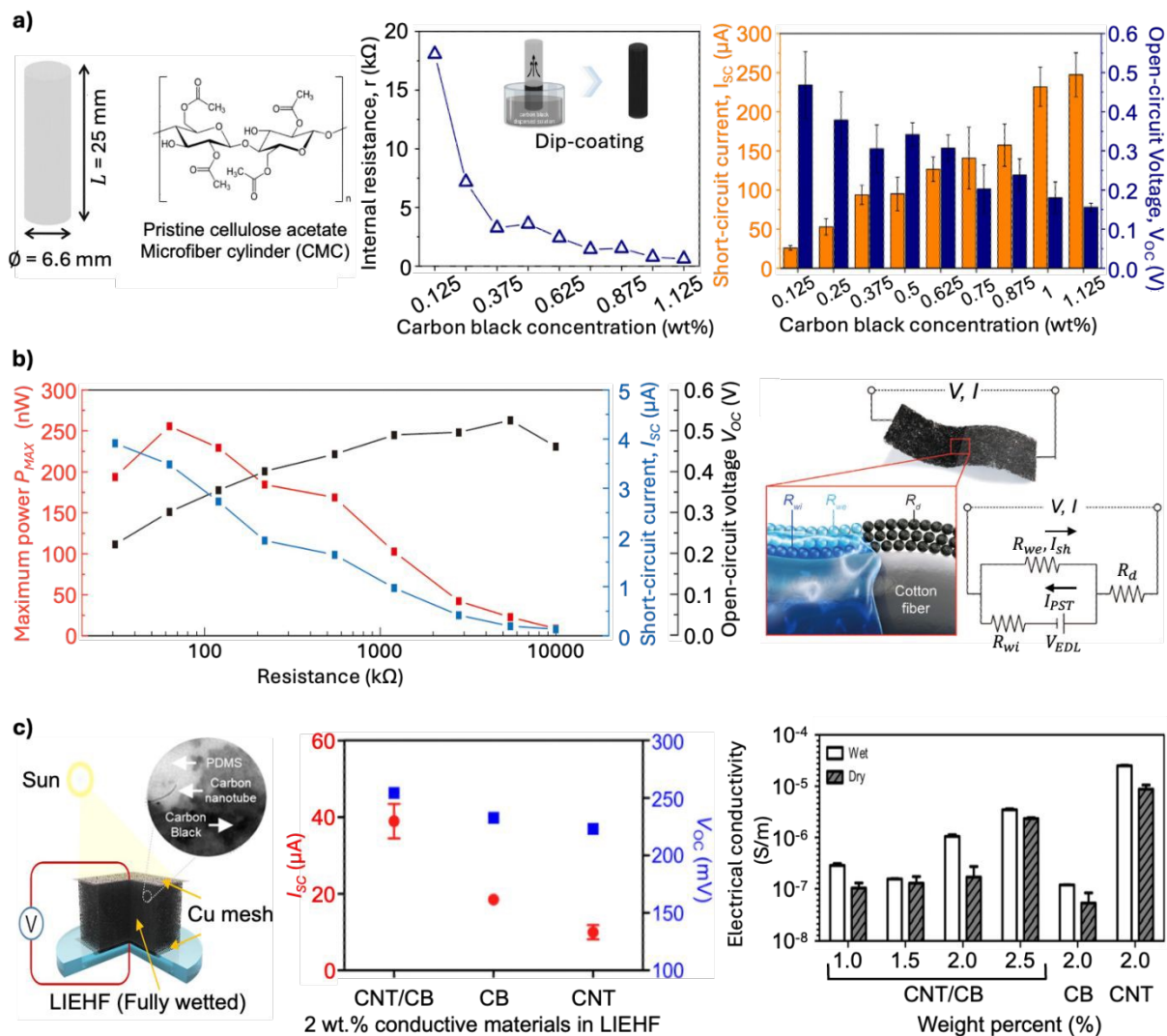


Figure 12. Output dependence on electronic conductivity in TIH devices. (a) Cellulose acetate microfiber cylinder (CMCG): device schematic, geometry, and molecular structure. Internal resistance decreases with increasing carbon-black loading (controlled via dip-coating from suspensions of different concentration; inset). Voltage and current exhibit opposite trends with carbon-black weight fraction. Reproduced with permission.⁵² Copyright 2023, Elsevier. (b) Cotton fabric coated with carbon black: maximum power, current, and voltage versus internal resistance, with an equivalent-circuit model illustrating how conductive “shunt” pathways reduce V_{OC} while increasing I_{sc} . Reproduced with permission.⁴² Copyright 2019, American Chemical Society. (c) Porous PDMS sponge with carbon black (CB) and CNT fillers: device concept (left), voltage/current output (middle), and conductivity versus CB/CNT composition (right). Reproduced with permission.⁷⁷ Copyright 2021, American Chemical Society.



1071

1072

1073

1074

1075

1076

1077

1078

1079

1080

1081

1082

1083

1084 **8.1 Voltage increases with resistivity, whereas current increases with conductivity**

1085 In Youm et al.'s study (**Figure 12a**), conductivity was tuned by changing the carbon black
 1086 loading in the deposited network. As the suspension was diluted, the device resistance increased
 1087 from $\sim 1 \text{ k}\Omega$ to $\sim 18 \text{ k}\Omega$.⁵² When a droplet of 3.3 M CaCl_2 was introduced near the device edge, the
 1088 peak voltage increased with resistance, whereas the current increased with conductivity. This
 1089 behavior aligns with a simple internal-resistance picture: higher conductivity facilitates charge
 1090 transport through the percolated network and therefore supports larger current, while higher
 1091 resistivity suppresses internal leakage and can allow a larger potential difference to be sustained
 1092 under open-circuit conditions.

1093 **8.2 Circuit models link conductivity to TIH output through shunt pathways**

1094 A closely related trend was reported by Yun et al (**Figure 12b**).⁴² using a cotton fabric
 1095 coated with conductive carbon black nanoparticles. In this system, conductivity was controlled by
 1096 repeated dip-coating to create multilayer carbon networks. The authors proposed an equivalent-
 1097 circuit model to rationalize why increasing conductivity can reduce voltage. Their physical picture
 1098 was that cotton's intrinsic wicking concentrates water near the cotton side, so the carbon layer
 1099 adjacent to the cotton becomes wetted and develops a strong EDL, whereas the outer carbon layers
 1100 remain comparatively dry and contribute primarily to electronic shunting rather than interfacial
 1101 charge separation. In this framework, increasing conductive loading preferentially strengthens
 1102 shunt pathways and dissipates the open-circuit voltage. Using this circuit representation, the
 1103 authors derived the following relations:

$$V_{OC} = V_{EDL} \left(1 - \frac{R_{wi}}{R_{wi} + R_{we}} \right) \quad (18)$$

1104

$$I_{SC} = \frac{V_{EDL}}{R_{wi} + R_d \left(1 + \frac{R_{wi}}{R_{we}} \right)} \quad (19)$$

1105 where R_{wi} is the resistance of the inner (wet) carbon layer, R_{we} is the resistance of the outer (dry)
 1106 carbon layer, and R_d represents resistance associated with the dry portion of the coated region.



1107 Increasing carbon loading decreases R_{we} as the exterior carbon network becomes more percolated.
1108 Equation (18) therefore predicts a reduction in V_{OC} as R_{we} decreases, while Equation (19) predicts
1109 increased I_{SC} as the effective internal resistance drops.

1110 This work is notable because it provided an explicit, testable framework that connects
1111 microstructural conduction pathways to macroscopic voltage–current trade-offs. A limitation is
1112 that the assumed spatial separation between “wet, EDL-active” and “dry, shunting” regions is
1113 difficult to verify directly. Spatially resolved measurements of hydration, potential, and ionic
1114 composition across thickness would strengthen the mechanistic basis and help generalize the
1115 model.

1116 **8.3 In composites, conductivity–output relationships are often nonmonotonic**

1117 In composite TIH systems, voltage and current frequently become nonmonotonic functions
1118 of substrate conductivity. This behavior reflects additional parameter couplings, including
1119 percolation thresholds, changes in surface chemistry and zeta potential, and the redistribution of
1120 water within the porous matrix. In these cases, conductivity is not an independent variable:
1121 increasing conductive content can simultaneously change hydrophilicity, pore connectivity, and
1122 interfacial charge regulation.

1123 Park et al. illustrated this complexity using a porous PDMS sponge incorporating carbon
1124 black and carbon nanotubes (CNTs) as conductive fillers (**Figure 12c**).⁷⁷ A slurry of PDMS with
1125 conductive additives was infiltrated into a sugar-powder template; after curing, the sugar was
1126 dissolved to yield an interconnected porous sponge. Because PDMS is intrinsically hydrophobic,
1127 the surface was plasma-treated to enable capillary pumping. The authors varied both the total filler
1128 content (1.0–2.5 wt%) and the filler composition (carbon black, CNTs, and 1:1 mixtures). As
1129 expected, conductivity increased with filler loading, and CNT-containing samples percolated more
1130 efficiently due to CNTs’ higher aspect ratio. Electrical output, however, did not track conductivity
1131 monotonically. Beyond a threshold filler content, slurry viscosity increased and infiltration into
1132 the sugar template became nonuniform, producing defects that blocked solution transport and
1133 degraded performance. Moreover, the sample with the highest conductivity (pure CNT) produced
1134 the lowest voltage, consistent with enhanced internal shunting. Notably, the highest voltage
1135 occurred at an intermediate composition (2 wt% CB/CNT mixture), whereas the most resistive
1136 sample (pure CB) did not yield the highest voltage either. The authors attributed the optimum to



1137 interfacial electrokinetics rather than conductivity alone: the intermediate mixed-filler sample
1138 exhibited the largest measured zeta potential, consistent with stronger counterion attraction and
1139 enhanced EDL-mediated selectivity. They also emphasized that excessive conductive loading can
1140 obstruct capillary pathways, reduce water infiltration, and weaken EDL formation, which can
1141 outweigh gains from lower electronic resistance.

1142 Across these studies, electrical conductivity is a key determinant of current generation, but
1143 it does not uniquely determine TIH voltage output. Increasing conductivity can increase I_{SC} while
1144 decreasing V_{OC} through internal leakage and shunt pathways. In composite systems, conductive
1145 additives also perturb pore structure, wetting, and surface charge regulation, producing
1146 nonmonotonic behavior and shifting the optimal loading. These results reinforce a practical design
1147 principle: in TIH, voltage is set primarily by interfacial electrokinetic strength (EDL formation,
1148 charge regulation, ion selectivity), whereas conductivity governs how efficiently that electric
1149 motive force is converted into usable current. Optimizing TIH performance therefore requires co-
1150 optimizing conductivity with capillary transport and interfacial chemistry, rather than tuning
1151 conductivity in isolation.

1152 9. Applications of TIH Harvesters

1153 With the rapid advancement in TIH device development, increasing attention has shifted
1154 from proof-of-concept demonstrations toward practical applications. Because TIH output can be
1155 amplified through modular integration of multiple units in series and parallel, recent studies have
1156 moved beyond powering light-emitting diodes and small electronic components to demonstrate
1157 operation of electrochemical reactors^{94,97,98}, ionic^{69,71,75,103,113} and chemical sensors^{129,130}. In this
1158 section, we highlight representative examples that illustrate how TIH output can be translated into
1159 useful functions and discuss the constraints that currently limit broader deployment.

1160 9.1 TIH-powered decentralized electrochemical processes and resource recovery

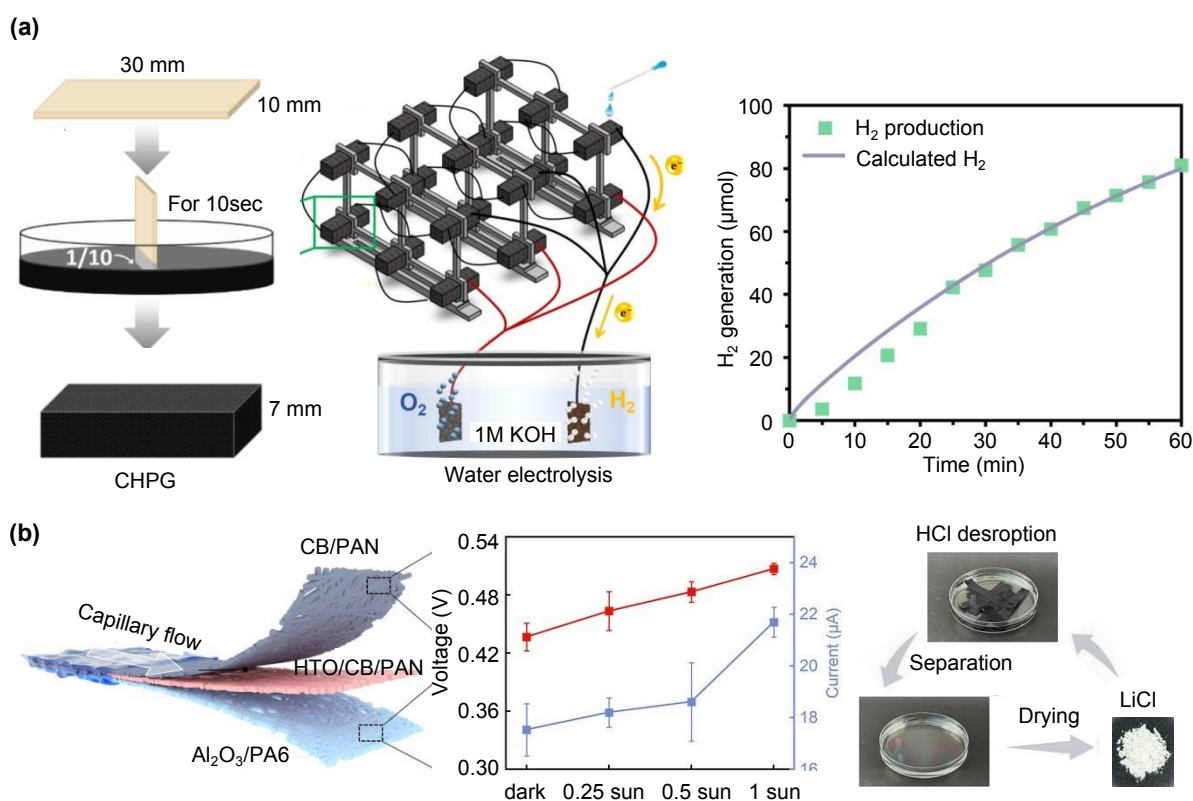
1161 One of the most promising application spaces for TIH is decentralized electrochemical
1162 operation. Early demonstrations showing TIH devices powering LEDs and small electronics
1163 established that evaporation-driven electricity can be harvested continuously under ambient
1164 conditions. More recent work has extended this concept to electrochemical systems, which require
1165 sustained electrical input to drive charge transfer reactions. These include water electrolysis,
1166 dialysis, and redox-based chemical conversions, and potentially critical mineral recovery.



1167

1168

1169



1170

1171

1172

1173

1174

1175

1176

1177

1178

1179

1180

1181

Figure 13. Representative and emerging applications of TIH devices on the resource recovery.

(a) TIH-powered water electrolysis and hydrogen generation. Right: fabrication schematic of a cellulose-sponge-based hydrovoltaic power generator (CHPG) and the electrolysis setup enabled by series/parallel CHPG arrays. Reproduced with permission.⁹⁸ Copyright 2024, Elsevier. **(b)** Integrated TIH power generation and lithium harvesting. Left: schematic of a device consisting of a CB/PAN layer (for TIH power generation), an HTO/CB/PAN layer (for lithium adsorption), and an Al₂O₃ substrate. Middle: power output as a function of sun light intensity. Right: lithium salt recovery process. After operation, the devices are immersed in HCl solution and then dried to obtain LiCl salt; the devices can be reused for both electricity generation and lithium harvesting. Reproduced with permission.¹³¹ Copyright 2025, Wiley VCH.



1182 9.1.1 TIH-powered water electrolysis

1183 In 2024, Jeong and co-workers demonstrated TIH-driven water splitting using commercial
1184 cosmetic removal pads coated with carbon black nanoparticles (**Figure 13a**).⁹⁸ Delivering CaCl₂
1185 solution to one edge of each unit produced electrical output that was scaled by series/parallel
1186 integration. The assembled array powered an electrolyser using a PCo/NF cathode for the
1187 hydrogen evolution reaction (HER) and a Co₃O₄/NiFe-LDH/NF anode for the oxygen evolution
1188 reaction (OER). By combining multiple units, the system achieved an open-circuit voltage of 2.09
1189 V and a short-circuit current of 3.11 mA, exceeding the practical threshold required for alkaline
1190 water splitting. The device produced approximately 80 μmol of H₂ over 1 hour. Although this
1191 demonstration required more than 30 individual TIH units, it highlights an important practical
1192 feature of the technology: output can be scaled through simple modular integration rather than by
1193 fabricating a single large monolith. More broadly, this result points to an opportunity for TIH in
1194 off-grid electrochemical processing, where distributed, low-cost generators could be coupled
1195 directly to catalytic electrodes, membranes, or microreactors.

1196 9.1.2 Coupled mineral recovery and energy harvesting

1197 Beyond powering electrochemical reactions, TIH architectures may also be integrated with
1198 resource-recovery functions. The growing demand for critical minerals such as lithium has
1199 intensified interest in extraction technologies with lower chemical and environmental footprints
1200 than conventional mining and refining.¹³² In this context, Lin et al. reported a combined TIH
1201 device and evaporation-driven lithium harvesting system (**Figure 13b**).¹³¹ The device consists of
1202 an Al₂O₃ substrate, a PAN fiber coated with protonated lithium titanate (HTO) and CB for lithium
1203 adsorption, and a PAN/CB layer for TIH power generation. Brine infiltrates the upper PAN-based
1204 layers, where Li⁺ is selectively adsorbed by the HTO-containing layer while capillary flow,
1205 enhanced by solar-thermal evaporation, drive water transport. Simultaneously, the upper PAN/CB
1206 layer generates electricity through the TIH mechanism. Under 1-sun illumination, the device
1207 produced 0.48 V and ~ 22 μA. After operation, adsorbed lithium was recovered by immersing the
1208 device in HCl solution to induce desorption, followed by drying to yield LiCl powder.

1209 This study highlights the possibility of using transpiration-inspired architectures to merge
1210 sustainable energy harvesting and mineral recovery within a single platform. However, the
1211 electricity generated by the TIH component was not yet actively used to drive an additional

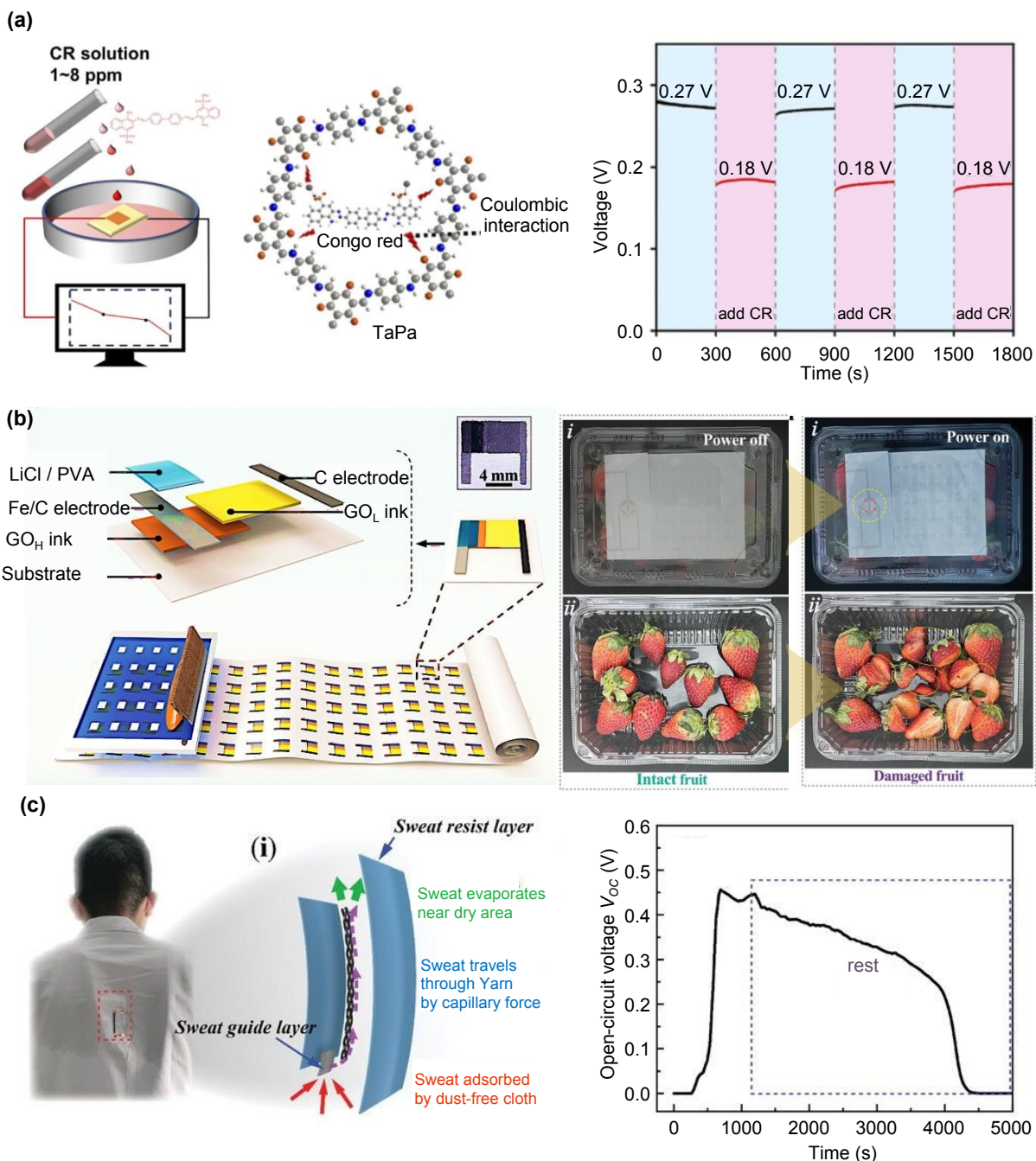


1212 electrochemical extraction step. This is an important direction for future work. For example,
1213 electrochemical lithium extraction based on battery-type electrode materials has previously been
1214 proposed for seawater and brine systems.¹³³ If the electrical energy required for such
1215 charge/discharge-assisted separations could be supplied locally by TIH devices, it would create a
1216 more tightly integrated nexus between water transport, energy harvesting, and critical mineral
1217 recovery.

1218 **9.2 TIH-powered distributed chemical sensing and environmental monitoring**

1219 In addition to acting as a power source, TIH devices can function as transducers because
1220 their electrical output is intrinsically sensitive to interfacial charge, ion transport, and
1221 environmental conditions. This feature makes TIH especially attractive for sensing applications,
1222 where the target analyte or surrounding environment modulates the same physicochemical
1223 processes responsible for electricity generation.

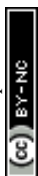




1224

1225 **Figure 14. Representative and emerging applications of TIH devices on self-powered sensing.**

1226 **(a)** Self-powered chemical sensing of Congo red (CR). Left: sensing concept. Middle: proposed
 1227 binding mechanism between the active ingredient TaPa and CR. Right: cycling tests show voltage
 1228 suppression upon CR binding. Reproduced with permission.¹²⁹ Copyright 2025, Elsevier. **(b)**
 1229 Flexible and scalable TIH device for agricultural product quality monitoring. Left: schematic
 1230 illustration of device components and screen-printed array on a flexible substrate. GO_H denotes a



1231 GO mixture with high activated carbon (AC) content, whereas GO_L denotes low AC content. Inset:
1232 optical image of a single device unit. Right: device powered by humidity increase caused by juice
1233 leaking from damaged fruit inside the package. Reproduced with permission.¹³⁴ Copyright 2024,
1234 Wiley VCH. (c) Wearable TIH device for sweat sensing, integrated into a fibrous strap and
1235 operated while attached to clothing. Green arrows indicate evaporation-driven liquid loss; red
1236 arrows indicate sweat inflow. Reproduced with permission.¹¹³ Copyright 2023, Wiley VCH.

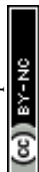
1237 9.2.1 Self-powered chemical sensing

1238 A direct example is chemical sensing based on analyte-induced changes in surface charge
1239 and electrokinetic transport. Zhou et al. developed a self-powered sensor for Congo red (CR) using
1240 a composite membrane of polyacrylonitrile (PAN) and a covalent organic framework (COF), TpPa
1241 (Figure 14a).¹²⁹ TpPa exhibits a strongly negative zeta potential (reported as -51.3 mV), which
1242 supports robust EDL formation and voltage generation. Because TaPa adsorbs CR, analyte binding
1243 alters the effective surface charge and reduces the zeta potential of the membrane. As CR loading
1244 increases, the device voltage decreases accordingly, enabling quantitative detection. Using this
1245 mechanism, the sensor detected CR concentrations from 1 to 33 ppm, demonstrating that TIH
1246 output can serve directly as a sensing signal without an external power supply.

1247 9.2.3. Environmental monitoring and smart packaging

1248 TIH devices are also highly sensitive to ambient variables such as humidity and
1249 temperature, as discussed in Section 7.¹³⁵ This environmental responsiveness suggests their utility
1250 as self-powered monitoring platforms. To move beyond simply observing output variation,
1251 however, TIH systems must be integrated with application-specific architectures that convert
1252 environmental changes into actionable information. An example was reported by Liu et al., who
1253 incorporated a TIH-based device into agricultural packaging to monitor product damage through
1254 humidity changes arising from juice leakage (Figure 14b).¹³⁴

1255 The device was fabricated on a flexible substrate by screen printing activated carbon (AC) and
1256 graphene oxide (GO)/AC composite inks to form functional micro/nanochannels. AC was also
1257 printed as the electrode material, after which a poly(vinyl alcohol) (PVA) gel electrolyte
1258 containing LiCl was deposited and dried. When humidity increases, water vapor is absorbed by
1259 the PVA gel, facilitating Li⁺ transport across the device and generating a voltage. Ion diffusion
1260 through the GO/AC channel sustains TIH-associated output. This mechanism enables practical



1261 damage indication in packaged agricultural products. When fruit or other produce is damaged,
1262 leaked juice raises the humidity inside the package, which activates the device and powers a red
1263 LED array to provide a clear visual warning. Such systems illustrate how TIH can be embedded
1264 into low-cost, disposable packaging for distributed quality control without requiring batteries or
1265 external electronics.

1266

1267 **9.3. Flexible and wearable TIH systems for real-time physiological monitoring**

1268 Wearable and epidermal electronics motivate self-powered platforms that can operate from
1269 physiological fluids. Sweat contains ions such as Na⁺, K⁺, and Ca²⁺, providing a naturally
1270 replenished electrolyte source during exercise or daily activity. Despite the promise of wearable
1271 sensors for real-time health monitoring, one of their persistent limitations is dependence on
1272 external power supplies, which often increase device weight, stiffness, and complexity.

1273 Because TIH systems have already demonstrated electricity generation from ionic aqueous
1274 electrolytes, we therefore reason that they must be well suited for sweat-powered wearable
1275 platforms. Indeed, several groups have explored TIH-like devices integrated into textiles or
1276 flexible substrates.¹³⁶ Luo et al. deposited carbon black and chemically oxidized multiwalled
1277 carbon nanotubes (MWCNTs) onto discarded mask straps and demonstrated electricity generation
1278 in several electrolytes, including NaCl, KCl, and LiCl solutions.¹¹³ In LiCl, the device
1279 generated >0.7 V and ~60 μA. The authors then integrated the device into clothing and tested it
1280 during vigorous exercise. As sweat was absorbed into the fibrous substrate, the device
1281 produced >0.4 V and continued generating output until the substrate dried during the subsequent
1282 rest period (**Figure 14c**). The signal persisted for nearly 1 hour, demonstrating that perspiration
1283 can sustain a continuous measurable signal in a wearable form factor. While this study did not yet
1284 close the loop by powering a specific on-body electronic system or performing quantitative analyte
1285 sensing, it establishes the fundamental feasibility of TIH operation in textiles and clarified the
1286 main engineering requirement: maintaining a stable wet–dry gradient or sustained evaporation
1287 pathway in a mechanically robust, wearable architecture.

1288 **9.4. From demonstrations to deployable systems**

1289 Although TIH remains an emerging technology, these examples demonstrate a clear
1290 progression from basic proof-of-concept demonstrations toward functional systems. Electrolysis
1291 highlights the ability of TIH arrays to achieve application-relevant voltage and current through
1292 modular scaling. Integrated lithium harvesting points to multifunctional platforms that combine
1293 water transport, energy generation, and resource recovery. Chemical sensing demonstrates that
1294 TIH can serve not only as a power source but also as a transduction mechanism, while packaging
1295 and wearable implementations illustrate how environmental or physiological inputs can be
1296 converted directly into actionable outputs. Going forward, the most consequential advances will
1297 likely arise from co-designing TIH architecture with the intended application. This includes
1298 packaging strategies that stabilize evaporation, materials engineering approaches that resist fouling
1299 in saline or biological fluids, and standardized load-matching methods that efficiently translate
1300 TIH output into usable electrical work. Progress in these areas will be essential for moving TIH
1301 from laboratory demonstrations toward practical platforms for distributed sensing, flexible
1302 electronics, and decentralized electrochemical technologies.

1304 10. Challenges and Outlook

1305 Transpiration-inspired hydrovoltaics (TIH) has advanced rapidly from early proof-of-
1306 concept demonstrations to devices that can sustain voltage output under ambient conditions and,
1307 through modular integration, power practical loads ranging from sensors to electrochemical
1308 reactions. At the same time, the field remains mechanistically and technologically immature. The
1309 central bottleneck is not simply achieving higher output, but establishing predictive theoretical
1310 frameworks that connect evaporation-driven water transport, evolving hydration states, and
1311 interfacial electrokinetics to measurable voltage, current, and power under load. In this section, we
1312 summarize key challenges and outline research opportunities that could transform TIH from an
1313 intriguing phenomenon into a designable and deployable energy-harvesting platform.

1314 10.1 Plant hydraulics as a blueprint for TIH design

1315 TIH has a distinctive advantage among emerging energy-harvesting concepts because the
1316 natural process it emulates, evaporation-driven water transport in plants, has been studied
1317 quantitatively for decades. Progress in TIH could be accelerated by treating these devices not



1318 simply as isolated porous films, but as engineered analogs of the soil-root-xylem-leaf continuum,
1319 and by translating established plant-hydraulics principles into device-level design rules.

1320 **Root-inspired intake.** Real deployment environments rarely provide an ideal, well-mixed
1321 water reservoir. Instead, water arrives intermittently, heterogeneously, and often in the presence
1322 of salts, particulates, or foulants. Root systems address this challenge through distributed uptake,
1323 moisture-seeking growth, and local buffering. TIH devices can borrow these principles through
1324 branched wicking networks that expand the capture area, graded wettability that preferentially
1325 draws water from wetter regions, and inlet layers that reduce salinity or fouling before water
1326 reaches the active transduction region.

1327 **Xylem-inspired transport.** Xylem balances high hydraulic conductance with resistance
1328 to cavitation through anisotropy, hierarchy, and compartmentalization. Comparable TIH
1329 architectures may include vertically aligned conduits for directional flow, hierarchical pore
1330 networks that combine rapid transport in larger pores with ion selectivity in smaller pores, and pit-
1331 like constrictions that suppress runaway drying and limit air invasion.

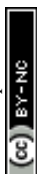
1332 **Leaf-inspired evaporation control.** Leaves maximize evaporative area while tightly
1333 regulating water loss through microstructure, surface chemistry, and boundary-layer effects. TIH
1334 can emulate this using passive, high-area evaporative interfaces that sustain a stable saturation
1335 gradient without drying the transport backbone, thereby improving both output and stability
1336 without reliance on external heating.

1337 Adopting plant-hydraulics metrics such as hydraulic conductance, saturation profile,
1338 capillary pressure, and failure threshold under evaporative demand could provide a common
1339 quantitative language linking water transport to electrokinetic output. This roots-xylem-leaf
1340 framework shifts scaling away from merely enlarging device area and toward co-designing intake,
1341 transport, and evaporation modules for robust and high-output operation.

1342

1343 **10.2 Treating evaporation as a quantitative driver rather than a qualitative prerequisite**

1344 Most mechanistic descriptions of TIH emphasize electrokinetic processes associated with
1345 EDL formation and selective ion transport, while treating evaporation primarily as a boundary
1346 condition that “maintains flow.” Yet almost all experimental studies identify evaporation as



1347 essential, and several report that it amplifies output beyond what classical electrokinetic streaming
1348 predicts. In plants, evaporation is not merely permissive. It generates a sustained water-potential
1349 gradient and can induce MPa-scale tension that stabilizes long-range flow. Translating this insight
1350 to TIH requires models that incorporate evaporation explicitly and quantitatively.

1351 A central gap is the lack of constitutive links between (1) evaporation flux at the device
1352 surface, (2) the resulting pressure distribution and saturation profile within the porous network,
1353 and (3) the electrokinetic source terms that generate voltage and current. Progress will likely
1354 require coupling porous-media transport (for example, Darcy flow with unsaturated permeability
1355 and capillary pressure–saturation relations) to ion transport and charge regulation (for example,
1356 Poisson–Nernst–Planck with surface charge that depends on pH and ionic strength), and then
1357 embedding these physics into an equivalent circuit or energy-balance framework that predicts
1358 measurable output under load. Establishing scaling laws that relate power density to measurable
1359 parameters such as evaporation rate, effective permeability, zeta potential, conductivity, and
1360 device hydration length would immediately enable rational design and fair comparison across
1361 studies.

1362 **10.3 Identifying optimal channel architectures through controlled structure–function** 1363 **comparisons**

1364 A wide range of channel conformations has been reported, including vertically aligned
1365 vascular templates, layered 2D nanochannels, honeycomb networks, random nanoporous packings,
1366 and hierarchical micro–nano structures. Each architecture can be argued to “improve” TIH
1367 performance, but the literature still lacks controlled comparisons that isolate geometry from
1368 chemistry and composition. As a result, it remains unclear which structural motif is optimal for a
1369 given goal: maximizing peak power density, maximizing stability under salinity, minimizing
1370 sensitivity to humidity, or sustaining operation under intermittent wetting.

1371 The path forward is to build structure–function maps under matched material chemistry.
1372 For example, families of architectures made from the same base material (or with standardized
1373 surface functionalization) could be compared while measuring hydraulic conductance, evaporation
1374 flux, saturation gradients, pore-size distributions, and effective ionic selectivity. Importantly,
1375 performance metrics should extend beyond open-circuit voltage and short-circuit current to include
1376 maximum power point under load, energy delivered per unit water evaporated, and lifetime under



1377 repeated cycling. Such datasets would reveal whether the best designs are those that maximize
1378 interfacial area, those that maximize directional conductance, or those that best stabilize a spatially
1379 persistent wet–dry asymmetry, and how these priorities shift with salinity and environment.

1380 **10.4 Distinguishing true hydrovoltaic output from electrochemical artifacts**

1381 One of the persistent sources of confusion in the hydrovoltaic field is the role of
1382 electrochemical reactions at the electrode-electrolyte interface. To clarify TIH as a distinct
1383 mechanism of power generation, it is essential to distinguish the redox reactions that are inherently
1384 required to convert ionic current into electronic current from additional electrochemical processes
1385 that effectively turn the system into a primary battery. As discussed in Section 4, classical
1386 streaming-potential systems inevitably involve electrode reactions that complete the circuit and
1387 enable charge transfer. At the same time, some studies intentionally introduce electrochemically
1388 active electrodes or redox-coupled electrolytes, for example by using reactive metals in saline
1389 solutions, to enhance output. Although such synergistic coupling may be useful for boosting
1390 practical performance, the distinction between intrinsic redox processes required for current
1391 conversion and parasitic or deliberately added battery-like chemistry must be stated explicitly.

1392 Even when studies employ carbon-based or nominally inert electrodes and provide
1393 supporting characterization, such as cyclic voltammetry or impedance spectroscopy, complete
1394 exclusion of electrochemical contributions remains difficult. This is especially true when
1395 electrodes contact electrolyte solutions under evaporation, where concentration gradients,
1396 dissolved oxygen gradients, and local pH shifts can develop over time. Because even small
1397 parasitic Faradaic currents can distort voltage-current behavior, rigorous controls are essential,
1398 particularly in studies claiming long-term stability, unusually high voltage, or operation in
1399 complex electrolytes.

1400 Stronger separation will likely require experimental protocols designed explicitly to falsify
1401 electrochemical explanations. Examples include: symmetric-electrode controls that suppress
1402 galvanic potentials, reference-electrode measurements to track local electrode potentials,
1403 electrolyte replacement experiments that hold conductivity constant while changing redox
1404 chemistry, and electrode-sealed devices that eliminate Faradaic redox processes (for non-
1405 traditional streaming potential TIH systems). Spatially resolved measurements of ionic
1406 concentration and pH along the device could also clarify whether output is linked to bulk gradients



1407 (which may drive electrochemical potentials) or to interfacial electrokinetic coupling in the porous
1408 network. Establishing “electrochemistry-free” benchmarks would strengthen the credibility of TIH
1409 as a distinct energy-harvesting modality and improve comparability across materials and designs.

1410 **10.5 Evaluating practicality through scaling and application-relevant metrics**

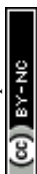
1411 Most TIH demonstrations remain at laboratory scale, often powering LEDs or intermittent
1412 low-power electronics. Moving toward practical deployment requires advances along two parallel
1413 routes: increasing power density of a single unit and scaling output through manufacturable arrays.
1414 Both routes depend on packaging and systems engineering, not only on materials.

1415 First, device packaging must stabilize the evaporation boundary condition and protect
1416 performance against fluctuations in humidity, wind, fouling, and mechanical disturbance. Semi-
1417 sealed architectures that maintain an internal water cycle, engineered “leaf” surfaces that maximize
1418 evaporation area without triggering premature drying, and antifouling designs for saline or biofluid
1419 environments will be essential for reliable operation. Second, scaling should be evaluated using
1420 application-relevant metrics: power delivered at the maximum power point, energy per unit
1421 evaporated water, volumetric and areal power density, cycling lifetime, and cost per watt for
1422 scalable fabrication. Third, integration with power management electronics (rectification,
1423 regulation, storage) and with specific loads (sensors, transmitters, electrochemical cells) will be
1424 required to translate TIH outputs into robust system-level function. Without these system-level
1425 considerations, improvements in open-circuit voltage or short-circuit current alone are unlikely to
1426 translate into practical utility.

1427 **10.6 Expanding material design through functionalization and interfacial engineering**

1428 A broadly accepted design principle in TIH is that high-performing materials should
1429 combine hydrophilicity with high surface charge, thereby promoting water transport, electric
1430 double-layer formation, and ionic current generation. Accordingly, widely studied materials such
1431 as carbon black, carbon nanotubes, graphene oxide, and metal oxides have been used extensively
1432 to exploit their favorable surface properties. Composite systems, including mixed carbon-
1433 black/CNT networks, have also been explored to combine complementary attributes.

1434 However, systematic chemical functionalization as a deliberate strategy for optimizing TIH
1435 performance remains underdeveloped. For example, oxidation of carbon materials can introduce



1436 hydrophilic functional groups that improve wettability, increase surface charge density, and
1437 strengthen ionic transport within the electric double layer. At the same time, oxidation can reduce
1438 intrinsic electrical conductivity, creating a tradeoff that must be optimized carefully. This suggests
1439 that TIH material design should move beyond simple material selection toward quantitative
1440 interfacial engineering that balances surface charge enhancement, wettability, pore accessibility,
1441 and electronic transport. In addition, covalent modification or crosslinking of base materials with
1442 functional molecules may provide a route to tailor interfacial properties more precisely. Such
1443 approaches could enable systematic tuning of acidity, ion affinity, antifouling behavior, and
1444 hydration stability, opening a broader materials-design space for TIH than is currently represented
1445 in the literature.

1446 **10.7 Integrating TIH with complementary systems for synergistic effect.**

1447 At present, many TIH studies emphasize either maximizing output or demonstrating that
1448 the signal changes in response to environmental stimuli. For instance, reduced output at high
1449 humidity is often cited as evidence that TIH may serve as a humidity sensor. However, most
1450 demonstrations remain at the level of passively observing output fluctuations rather than
1451 converting those fluctuations into actionable functionality. True practical value will come not from
1452 simply reading a changing signal, but from integrating TIH with complementary systems that
1453 actively communicate, regulate, or exploit that signal.

1454 One promising direction is agricultural monitoring. As discussed in Section 6, both tree
1455 physiology and TIH device performance are strongly influenced by water availability and salinity.
1456 This analogy suggests the possibility of TIH-based platforms for monitoring soil moisture and salt
1457 stress in agricultural settings. During drought, reduced soil water content and concurrent changes
1458 in ion concentration would alter TIH output, potentially allowing localized detection of water
1459 deficiency or nutrient imbalance. Such distributed sensing could help farmers direct irrigation or
1460 fertilization more precisely, rather than applying resources uniformly across an entire field.
1461 Another opportunity lies in coupling TIH with solar desalination or water-treatment technologies.
1462 Ocean-deployed or brine-exposed TIH arrays could benefit from the abundant water supply, while
1463 solar desalination systems already rely on porous micro-nano architectures with high surface area
1464 for water transport and rapid evaporation. Because these same structural features are also favorable



1465 for TIH, integrating the two systems could create synergistic platforms for concurrent water
1466 purification and electricity generation.

1467 More broadly, the most compelling near-term niches for TIH may be distributed, low-
1468 power settings where water is already present and evaporation is unavoidable, such as soil and
1469 infrastructure monitoring, wearable or textile-based sensing, and water-treatment interfaces. In
1470 these contexts, TIH may be most valuable not as a competitor to batteries or photovoltaics on
1471 energy density, but as a maintenance-free trickle-power source that converts an ambient water flux
1472 into persistent electrical functionality.

1473 TIH stands at an important transition point. The field has clearly established that
1474 evaporation-driven water transport through charged porous media can generate useful electrical
1475 output, yet it has not fully matured into a predictive engineering discipline. The next phase of
1476 progress will depend on moving beyond isolated demonstrations toward quantitative frameworks,
1477 controlled benchmarking, and application-driven design. If these challenges are addressed, TIH
1478 could evolve into a distinctive class of energy-harvesting technologies that leverages ubiquitous
1479 water fluxes for persistent, low-power operation in environments where conventional power
1480 sources are impractical or undesirable.

1481

1482 **11. Conclusion**

1483 Evaporation is involved in one of the most powerful and spatially distributed energy
1484 conversion processes on Earth, yet it has historically been harvested only after the water cycle
1485 concentrates that energy into macroscopic motion, as in rivers and hydroelectric plants.
1486 Transpiration-inspired hydrovoltaics offers a complementary route: harvesting energy closer to the
1487 source by rectifying evaporation-sustained capillary transport into electrical output within
1488 microstructured and nanostructured solids. By drawing a direct analogy to tree hydraulics, TIH
1489 devices exploit the same core ingredients that make transpiration effective, including capillary-
1490 driven water supply, persistent evaporation at exposed interfaces, and strong water–solid
1491 interactions under confinement. Across the literature, TIH systems have demonstrated that voltage
1492 and current can be sustained under ambient conditions, can be tuned through geometry,
1493 microarchitecture, conductivity, and environment, and can be scaled through modular integration
1494 to power practical functions such as sensing and electrochemical reactions. At the same time, the



1495 field faces clear mechanistic and engineering challenges. The central need is a predictive
1496 framework that couples evaporation-driven unsaturated flow to interfacial charge regulation and
1497 ion transport, enabling quantitative scaling laws and principled optimization. Controlled
1498 comparisons of channel architectures, rigorous exclusion of electrochemical artefacts, and
1499 application-relevant performance metrics will be essential for establishing TIH as a mature energy-
1500 harvesting technology. More broadly, TIH reframes evaporation from a loss mechanism into an
1501 opportunity for distributed energy conversion. If the community can unify transpiration physics
1502 with electrokinetic transduction in a quantitative, designable framework, TIH could emerge as a
1503 new paradigm for low-cost, distributed power in the water–energy nexus, enabling autonomous
1504 devices that operate where moisture and evaporation are naturally abundant.

1505



1506 Author contributions

1507 **ATL:** Conceptualization, Writing-Review & Editing, Supervision, Writing-Original Draft
1508 Project Administration. **JW:** Conceptualization, Investigation, Writing-Original Draft,
1509 Visualization.

1510 Conflicts of interest

1511 There are no conflicts to declare.

1512 Data availability

1513 The data supporting findings of the current work is available at the following URL/DOI:
1514 @@@

1515 Acknowledgements

1516 The authors are grateful to NSF for the award #2243104, CENTER FOR COMPLEX
1517 PARTICLE SYSTEMS (COMPASS). The work was also supported by ACS PRF Doctoral New
1518 Investigator grant (Grant Number: 66979-DNI10). We thank the Michigan Materials Research
1519 Institute (MMRI). The authors also wish to acknowledge the support from the University of
1520 Michigan Institute of Energy Studies and the Bold Challenges Boost program.

1521
1522 References

- 1523 1. Stephens, G. L. *et al.* An update on Earth's energy balance in light of the latest global
1524 observations. *Nat. Geosci.* **5**, 691–696 (2012).
- 1525 2. Scanlon, B. R. *et al.* Global water resources and the role of groundwater in a resilient water
1526 future. *Nat. Rev. Earth Environ.* **4**, 87–101 (2023).
- 1527 3. Cavusoglu, A.-H., Chen, X., Gentine, P. & Sahin, O. Potential for natural evaporation as a
1528 reliable renewable energy resource. *Nat. Commun.* **8**, 617 (2017).
- 1529 4. Frijns, J., Hofman, J. & Nederlof, M. The potential of (waste)water as energy carrier. *Energy*
1530 *Convers. Manag.* **65**, 357–363 (2013).



- 1531 5. Wang, X. *et al.* Hydrovoltaic technology: from mechanism to applications. *Chem. Soc. Rev.*
1532 **51**, 4902–4927 (2022).
- 1533 6. Evans, A., Strezov, V. & Evans, T. J. Assessment of sustainability indicators for renewable
1534 energy technologies. *Renew. Sustain. Energy Rev.* **13**, 1082–1088 (2009).
- 1535 7. Li, Y., Zhao, G., Allen, G. H. & Gao, H. Diminishing storage returns of reservoir
1536 construction. *Nat. Commun.* **14**, 3203 (2023).
- 1537 8. Nagata, Y., Usui, K. & Bonn, M. Molecular Mechanism of Water Evaporation. *Phys. Rev.*
1538 *Lett.* **115**, 236102 (2015).
- 1539 9. Zhao, F., Guo, Y., Zhou, X., Shi, W. & Yu, G. Materials for solar-powered water
1540 evaporation. *Nat. Rev. Mater.* **5**, 388–401 (2020).
- 1541 10. Dao, V.-D., Vu, N. H., Thi Dang, H.-L. & Yun, S. Recent advances and challenges for water
1542 evaporation-induced electricity toward applications. *Nano Energy* **85**, 105979 (2021).
- 1543 11. Ashrafi, A. Quantum Confinement: An Ultimate Physics of Nanostructures.
- 1544 12. Hamaguchi, C. *Basic Semiconductor Physics*. (Springer International Publishing, Cham,
1545 2017). doi:10.1007/978-3-319-66860-4.
- 1546 13. Wang, Y. D. Solar-driven abnormal evaporation of nanocomfined water. *Sci. Adv.* **10**,
1547 (2012).
- 1548 14. Liu, X. *et al.* Power generation from ambient humidity using protein nanowires. *Nature* **578**,
1549 550–554 (2020).
- 1550 15. Liu, K. *et al.* Induced Potential in Porous Carbon Films through Water Vapor Absorption.
1551 *Angew. Chem. Int. Ed.* **55**, 8003–8007 (2016).
- 1552 16. Scharwies, J. D. & Dinneny, J. R. Water transport, perception, and response in plants. *J.*
1553 *Plant Res.* **132**, 311–324 (2019).



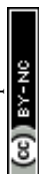
- 1554 17. Brown, H. R. & Sutton, A. P. Trees suck. Notes on the physics of transpiration in trees.
1555 *Prog. Biophys. Mol. Biol.* **195**, 71–86 (2025).
- 1556 18. Morrow, M. H., Maria, & Algiers, K. Botany. in *Botany* (ASCCC Open Educational
1557 Resources Initiative).
- 1558 19. Wheeler, T. D. & Stroock, A. D. The transpiration of water at negative pressures in a
1559 synthetic tree. *Nature* **455**, 208–212 (2008).
- 1560 20. Herbert, E., Balibar, S. & Caupin, F. Cavitation pressure in water. *Phys. Rev. E* **74**, 041603
1561 (2006).
- 1562 21. Boatwright, A., Hughes, S. & Barry, J. The height limit of a siphon. *Sci. Rep.* **5**, 16790
1563 (2015).
- 1564 22. *Geotechnical Fundamentals for Addressing New World Challenges*. (Springer International
1565 Publishing, Cham, 2019). doi:10.1007/978-3-030-06249-1.
- 1566 23. Powers, W. L. Physical Edaphology: The Physics of Irrigated and Non-irrigated Soils: By
1567 Sterling A. Taylor, and Gaylen L. Ashcroft. W. H. Freeman and Co., 660 Market Street, San
1568 Francisco, Calif. 94104. 1972. 533 pages. 279 illus. 46 tables. \$17.50. *J. Environ. Qual.* **3**,
1569 188–188 (1974).
- 1570 24. Han, S., Kim, W., Lee, H. J., Joyce, R. & Lee, J. Continuous and Real-Time Measurement of
1571 Plant Water Potential Using an AAO-Based Capacitive Humidity Sensor for Irrigation
1572 Control. *ACS Appl. Electron. Mater.* **4**, 5922–5932 (2022).
- 1573 25. Jain, P. *et al.* A minimally disruptive method for measuring water potential in planta using
1574 hydrogel nanoreporters. *Proc. Natl. Acad. Sci.* **118**, e2008276118 (2021).



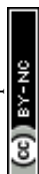
- 1575 26. Han, S., Kim, W., Lee, H. J., Joyce, R. & Lee, J. Continuous and Real-Time Measurement of
1576 Plant Water Potential Using an AAO-Based Capacitive Humidity Sensor for Irrigation
1577 Control. *ACS Appl. Electron. Mater.* **4**, 5922–5932 (2022).
- 1578 27. Jain, P. Localized measurements of water potential reveal large loss of conductance in living
1579 tissues of maize leaves.
- 1580 28. Shi, W. *et al.* Passive water ascent in a tall, scalable synthetic tree. *Sci. Rep.* **10**, 230 (2020).
- 1581 29. Poudel, S., Zou, A. & Maroo, S. C. Disjoining pressure driven transpiration of water in a
1582 simulated tree. *J. Colloid Interface Sci.* **616**, 895–902 (2022).
- 1583 30. Tyree, M. T. The Cohesion-Tension theory of sap ascent: current controversies. *J. Exp. Bot.*
1584 <https://doi.org/https://doi.org/10.1093/jxb/48.10.1753>
1585 doi:<https://doi.org/10.1093/jxb/48.10.1753>.
- 1586 31. Tyree, M. T. The Cohesion-Tension theory of sap ascent: current controversies.
- 1587 32. Zimmermann, U., Schneider, H., Wegner, L. H. & Haase, A. Water ascent in tall trees: does
1588 evolution of land plants rely on a highly metastable state? *New Phytol.* **162**, 575–615 (2004).
- 1589 33. Chen, I.-T. *et al.* Stability Limit of Water by Metastable Vapor–Liquid Equilibrium with
1590 Nanoporous Silicon Membranes. *J. Phys. Chem. B* **120**, 5209–5222 (2016).
- 1591 34. Koch, G. W., Sillett, S. C., Jennings, G. M. & Davis, S. D. The limits to tree height. *Nature*
1592 **428**, 851–854 (2004).
- 1593 35. Van P. Carey. *Liquid-Vapor Phase-Change Phenomena*. (CRC Press, Boca Raton, 2020).
- 1594 36. Xue, G. *et al.* Water-evaporation-induced electricity with nanostructured carbon materials.
1595 *Nat. Nanotechnol.* **12**, 317–321 (2017).
- 1596 37. Yin, J. *et al.* Generating electricity by moving a droplet of ionic liquid along graphene. *Nat.*
1597 *Nanotechnol.* **9**, 378–383 (2014).



- 1598 38. Yin, J. *et al.* Waving potential in graphene. *Nat. Commun.* **5**, 3582 (2014).
- 1599 39. Liu, A. T. *et al.* Electrical Energy Generation via Reversible Chemical Doping on Carbon
1600 Nanotube Fibers. *Adv. Mater.* **28**, 9752–9757 (2016).
- 1601 40. Kunai, Y. *et al.* Observation of the Marcus Inverted Region of Electron Transfer from
1602 Asymmetric Chemical Doping of Pristine (n, m) Single-Walled Carbon Nanotubes. *J. Am.*
1603 *Chem. Soc.* **139**, 15328–15336 (2017).
- 1604 41. Liu, A. T. *et al.* Direct Electricity Generation Mediated by Molecular Interactions with Low
1605 Dimensional Carbon Materials—A Mechanistic Perspective. *Adv. Energy Mater.* **8**, 1802212
1606 (2018).
- 1607 42. Yun, T. G., Bae, J., Rothschild, A. & Kim, I.-D. Transpiration Driven Electrokinetic Power
1608 Generator. *ACS Nano* **13**, 12703–12709 (2019).
- 1609 43. Yoon, S. G. *et al.* Natural Evaporation-Driven Ionovoltaic Electricity Generation. *ACS Appl.*
1610 *Electron. Mater.* **1**, 1746–1751 (2019).
- 1611 44. Stern, O. ZUR THEORIE DER ELEKTROLYTISCHEN DOPPELSCHICHT. *Z. Für*
1612 *Elektrochem. Angew. Phys. Chem.* **30**, 508–516 (1924).
- 1613 45. Quincke, G. Ueber die Fortführung materieller Theilchen durch strömende Elektrizität. *Ann.*
1614 *Phys.* **189**, 513–598 (1861).
- 1615 46. Wall, S. The history of electrokinetic phenomena. *Curr. Opin. Colloid Interface Sci.* **15**,
1616 119–124 (2010).
- 1617 47. Van Der Heyden, F. H. J., Stein, D. & Dekker, C. Streaming Currents in a Single
1618 Nanofluidic Channel. *Phys. Rev. Lett.* **95**, 116104 (2005).
- 1619 48. Mooney, M. Electrophoresis and the Diffuse Ionic Layer. *J. Phys. Chem.* **35**, 331–344
1620 (1931).



- 1621 49. Chaurasia, S., Kumar, R., Tabrizizadeh, T., Liu, G. & Stampelcoskie, K. All-Weather-
1622 Compatible Hydrovoltaic Cells Based on Al₂O₃ TLC Plates. *ACS Omega* **7**, 2618–2623
1623 (2022).
- 1624 50. Bae, J., Yun, T. G., Suh, B. L., Kim, J. & Kim, I.-D. Self-operating transpiration-driven
1625 electrokinetic power generator with an artificial hydrological cycle. *Energy Environ. Sci.* **13**,
1626 527–534 (2020).
- 1627 51. Yoon, S. G. *et al.* Evaporative electrical energy generation via diffusion-driven ion-electron-
1628 coupled transport in semiconducting nanoporous channel. *Nano Energy* **80**, 105522 (2021).
- 1629 52. Youm, J. *et al.* Highly increased hydrovoltaic power generation via surfactant optimization
1630 of carbon black solution for cellulose microfiber cylindrical generator. *Surf. Interfaces* **38**,
1631 102853 (2023).
- 1632 53. Cazzolla Gatti, R. *et al.* The number of tree species on Earth. *Proc. Natl. Acad. Sci.* **119**,
1633 e2115329119 (2022).
- 1634 54. Nabeshima, E., Kubo, T. & Hiura, T. Variation in tree diameter growth in response to the
1635 weather conditions and tree size in deciduous broad-leaved trees. *For. Ecol. Manag.* **259**,
1636 1055–1066 (2010).
- 1637 55. Liang, R., Sun, Y., Qiu, S., Wang, B. & Xie, Y. Relative effects of climate, stand
1638 environment and tree characteristics on annual tree growth in subtropical *Cunninghamia*
1639 *lanceolata* forests. *Agric. For. Meteorol.* **342**, 109711 (2023).
- 1640 56. Fernández-de-Uña, L., Martínez-Vilalta, J., Poyatos, R., Mencuccini, M. & McDowell, N. G.
1641 The role of height-driven constraints and compensations on tree vulnerability to drought.
1642 *New Phytol.* **239**, 2083–2098 (2023).



- 1643 57. D. Whitehead, W.R.N. Edwards, & P.G. Jarvis. Conducting sapwood area, foliage area, and
1644 permeability in mature trees of *Picea sitchensis* and *Pinus contorta*. *Can. J. For. Res.* 940–947
1645 (1984) doi:<https://doi.org/10.1139/x84-166>.
- 1646 58. Fernández-de-Uña, L., Martínez-Vilalta, J., Poyatos, R., Mencuccini, M. & McDowell, N. G.
1647 The role of height-driven constraints and compensations on tree vulnerability to drought.
1648 *New Phytol.* **239**, 2083–2098 (2023).
- 1649 59. *Size- and Age-Related Changes in Tree Structure and Function*. vol. 4 (Springer
1650 Netherlands, Dordrecht, 2011).
- 1651 60. Ambrose, A. R. *et al.* Effects of height on treetop transpiration and stomatal conductance in
1652 coast redwood (*Sequoia sempervirens*). *Tree Physiol.* **30**, 1260–1272 (2010).
- 1653 61. Rosell, J. A., Gleason, S., Méndez-Alonzo, R., Chang, Y. & Westoby, M. Bark functional
1654 ecology: evidence for tradeoffs, functional coordination, and environment producing bark
1655 diversity. *New Phytol.* **201**, 486–497 (2014).
- 1656 62. Tumber-Dávila, S. J., Schenk, H. J., Du, E. & Jackson, R. B. Plant sizes and shapes above
1657 and belowground and their interactions with climate. *New Phytol.* **235**, 1032–1056 (2022).
- 1658 63. Fan, Y., Miguez-Macho, G., Jobbágy, E. G., Jackson, R. B. & Otero-Casal, C. Hydrologic
1659 regulation of plant rooting depth. *Proc. Natl. Acad. Sci.* **114**, 10572–10577 (2017).
- 1660 64. Tariq, A. *et al.* Plant root mechanisms and their effects on carbon and nutrient accumulation
1661 in desert ecosystems under changes in land use and climate. *New Phytol.* **242**, 916–934
1662 (2024).
- 1663 65. Li, X. *et al.* Ion-selective vermiculite nanochannel membrane with water anchoring effect for
1664 efficient energy recovery from water evaporation. *J. Membr. Sci.* **718**, 123698 (2025).



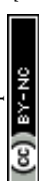
- 1665 66. Shao, C. *et al.* Large-Scale Production of Flexible, High-Voltage Hydroelectric Films Based
1666 on Solid Oxides. *ACS Appl. Mater. Interfaces* **11**, 30927–30935 (2019).
- 1667 67. Chi, J. *et al.* Harvesting Water-Evaporation-Induced Electricity Based on Liquid–Solid
1668 Triboelectric Nanogenerator. *Adv. Sci.* **9**, 2201586 (2022).
- 1669 68. Jiao, S. *et al.* Evaporation Driven Hydrovoltaic Generator Based on Nano-Alumina-Coated
1670 Polyethylene Terephthalate Film. *Polymers* **15**, 4079 (2023).
- 1671 69. Li, L. *et al.* A novel, flexible dual-mode power generator adapted for wide dynamic range of
1672 the aqueous salinity. *Nano Energy* **85**, 105970 (2021).
- 1673 70. Li, L. *et al.* Sustainable and flexible hydrovoltaic power generator for wearable sensing
1674 electronics. *Nano Energy* **72**, 104663 (2020).
- 1675 71. Shi, X. *et al.* A Kirigami-Driven Stretchable Paper-Based Hydrovoltaic Electricity
1676 Generator. *Adv. Funct. Mater.* 2419753 (2025) doi:10.1002/adfm.202419753.
- 1677 72. Wang, X. *et al.* Composite laminar membranes for electricity generation from water
1678 evaporation. *Nano Res.* **17**, 307–311 (2024).
- 1679 73. Eun, J. & Jeon, S. Janus Membrane-Based Hydrovoltaic Power Generation with Enhanced
1680 Performance under Suppressed Evaporation Conditions. *ACS Appl. Mater. Interfaces* **15**,
1681 50126–50133 (2023).
- 1682 74. Tabrizzadeh, T. *et al.* Water-Evaporation-Induced Electric Generator Built from Carbonized
1683 Electrospun Polyacrylonitrile Nanofiber Mats. *ACS Appl. Mater. Interfaces* **13**, 50900–
1684 50910 (2021).
- 1685 75. Wang, Y. *et al.* 3D dendritic hierarchically gradient nanoflowers *in situ* grown on conductive
1686 substrates for efficient hydrovoltaic power generation. *Energy Environ. Sci.* **17**, 4780–4793
1687 (2024).



- 1688 76. Cao, M. *et al.* Ambient-Dried Nanocellulose Composite Aerogels for Enhanced Hydrovoltaic
1689 Electricity Generation. *Adv. Funct. Mater.* 2418823 (2024) doi:10.1002/adfm.202418823.
- 1690 77. Park, J. H., Park, S. H., Lee, J. & Lee, S. J. Solar Evaporation-Based Energy Harvesting
1691 Using a Leaf-Inspired Energy-Harvesting Foam. *ACS Sustain. Chem. Eng.* **9**, 5027–5037
1692 (2021).
- 1693 78. Yang, S. *et al.* Ionic Hydrogel for Efficient and Scalable Moisture-Electric Generation. *Adv.*
1694 *Mater.* **34**, 2200693 (2022).
- 1695 79. Yuan, W. *et al.* Scalable MXene/Sepiolite film-based hydrovoltaic generators with
1696 outstanding output power. *Chem. Eng. J.* **499**, 155952 (2024).
- 1697 80. Lintunen, A. & Kalliokoski, T. The effect of tree architecture on conduit diameter and
1698 frequency from small distal roots to branch tips in *Betula pendula*, *Picea abies* and *Pinus*
1699 *sylvestris*. *Tree Physiol.* **30**, 1433–1447 (2010).
- 1700 81. Lv, S. *et al.* Xylem anatomy differentiation explains coordinated variation of economic and
1701 hydraulic traits in urban tree species. *BMC Plant Biol.* **25**, 1549 (2025).
- 1702 82. Hudson, P. J., Razanatsoa, J. & Feild, T. S. Early vessel evolution and the diversification of
1703 wood function: Insights from Malagasy Canellales. *Am. J. Bot.* **97**, 80–93 (2010).
- 1704 83. Hacke, U. G., Sperry, J. S. & Pittermann, J. Efficiency Versus Safety Tradeoffs for Water
1705 Conduction in Angiosperm Vessels Versus Gymnosperm Tracheids. in *Vascular Transport*
1706 *in Plants* 333–353 (Elsevier, 2005). doi:10.1016/B978-012088457-5/50018-6.
- 1707 84. Zhang, M. *et al.* Comparison of wood physical and mechanical traits between major
1708 gymnosperm and angiosperm tree species in China. *Wood Sci. Technol.* **51**, 1405–1419
1709 (2017).



- 1710 85. Williams, C. B. *et al.* Axial variation of xylem conduits in the Earth's tallest trees. *Trees* **33**,
1711 1299–1311 (2019).
- 1712 86. Jansen, S., Baas, P., Gasson, P., Lens, F. & Smets, E. Variation in xylem structure from
1713 tropics to tundra: Evidence from vestured pits. *Proc. Natl. Acad. Sci.* **101**, 8833–8837
1714 (2004).
- 1715 87. Zhou, X. *et al.* Harvesting Electricity from Water Evaporation through Microchannels of
1716 Natural Wood. *ACS Appl. Mater. Interfaces* **12**, 11232–11239 (2020).
- 1717 88. Yu, S. *et al.* Interlayer mediated water motion-induced ionovoltaic electricity generation.
1718 *Nano Energy* **123**, 109345 (2024).
- 1719 89. Anwar, T. & Tagliabue, G. Salinity-dependent interfacial phenomena toward hydrovoltaic
1720 device optimization. *Device* **2**, 100287 (2024).
- 1721 90. Garemark, J. *et al.* Advancing Hydrovoltaic Energy Harvesting from Wood through Cell
1722 Wall Nanoengineering. *Adv. Funct. Mater.* **33**, 2208933 (2023).
- 1723 91. Shao, B. *et al.* Bioinspired Hierarchical Nanofabric Electrode for Silicon Hydrovoltaic
1724 Device with Record Power Output. *ACS Nano* **15**, 7472–7481 (2021).
- 1725 92. Liu, Z. *et al.* Tortuosity regulation of two-dimensional nanofluidic films for water
1726 evaporation-induced electricity generation. *Nano Res.* **17**, 6192–6202 (2024).
- 1727 93. Wu, M. *et al.* Printed Honeycomb-Structured Reduced Graphene Oxide Film for Efficient
1728 and Continuous Evaporation-Driven Electricity Generation from Salt Solution. *ACS Appl.*
1729 *Mater. Interfaces* **13**, 26989–26997 (2021).
- 1730 94. Ding, T. *et al.* All-Printed Porous Carbon Film for Electricity Generation from
1731 Evaporation-Driven Water Flow. *Adv. Funct. Mater.* **27**, 1700551 (2017).



- 1732 95. Wu, M. *et al.* High evaporation rate and electrical conductivity synergistically boosting
1733 porous rGO/CNT Film for water evaporation-driven electricity generation. *Nano Energy*
1734 **116**, 108771 (2023).
- 1735 96. Ji, B. *et al.* Intelligent multiple-liquid evaporation power generation platform using
1736 distinctive Jaboticaba-like carbon nanosphere@TiO₂ nanowires. *J. Mater. Chem. A* **7**, 6766–
1737 6772 (2019).
- 1738 97. Lee, S.-H. *et al.* Cost-effective moisture-induced electrical power generators for sustainable
1739 electro dialysis desalination. *Nano Energy* **126**, 109683 (2024).
- 1740 98. Lee, S.-H. *et al.* A novel water electrolysis hydrogen production system powered by a
1741 renewable hydrovoltaic power generator. *Chem. Eng. J.* **495**, 153411 (2024).
- 1742 99. Lee, S.-H. *et al.* Water-Based Generators with Cellulose Acetate: Uncovering the
1743 Mechanisms of Power Generation. *Polymers* **16**, 433 (2024).
- 1744 100. Li, J. *et al.* Surface functional modification boosts the output of an evaporation-driven
1745 water flow nanogenerator. *Nano Energy* **58**, 797–802 (2019).
- 1746 101. Li, J., Dai, Y., Jiao, S. & Liu, X. MOFs/Ketjen Black-Coated Filter Paper for
1747 Spontaneous Electricity Generation from Water Evaporation. *Polymers* **14**, 3509 (2022).
- 1748 102. Li, L. *et al.* Ionovoltaic natural evaporation-induced electrical energy harvesting for green
1749 hydrogen generation. *Nano Energy* **136**, 110731 (2025).
- 1750 103. Li, L. *et al.* A Flexible Tough Hydrovoltaic Coating for Wearable Sensing Electronics.
1751 *Adv. Mater.* **35**, 2304099 (2023).
- 1752 104. Hossain, N. *et al.* HYDROVOLTAIC ENERGY HARVESTING FROM NUT SHELLS.
1753 Preprint at <https://doi.org/10.22541/au.172674720.00693759/v1> (2024).



- 1754 105. Liu, Y. *et al.* A fabric-based hydrovoltaic electricity generator with multi-component
1755 carbon black for sustainable energy output. *RSC Adv.* **14**, 18832–18837 (2024).
- 1756 106. Liu, Z. *et al.* Self-floating Janus hydrovoltaics for sustainable electricity generation. *J.*
1757 *Power Sources* **628**, 235934 (2025).
- 1758 107. Tian, B. *et al.* Integrating reduced graphene oxides and PPy nanoparticles for enhanced
1759 electricity from water evaporation. *Int. J. Smart Nano Mater.* **14**, 230–242 (2023).
- 1760 108. Wang, Y. *et al.* Graphene oxide and carbon black synergistic coated cotton fabric for
1761 enhancing energy harvesting from water droplets. *Carbon* **223**, 119008 (2024).
- 1762 109. Yuan, R. *et al.* Hermetic hydrovoltaic cell sustained by internal water circulation. *Nat.*
1763 *Commun.* **15**, 9796 (2024).
- 1764 110. Yun, T. G. *et al.* Ion-permselective conducting polymer-based electrokinetic generators
1765 with maximized utility of green water. *Nano Energy* **94**, 106946 (2022).
- 1766 111. Zhang, G. *et al.* Harvesting environment energy from water-evaporation over free-
1767 standing graphene oxide sponges. *Carbon* **148**, 1–8 (2019).
- 1768 112. Zhang, X. *et al.* Fabrication and study of a high output power flexible fabric hydrovoltaic
1769 generator. *J. Mater. Chem. A* **11**, 26173–26182 (2023).
- 1770 113. Luo, G. *et al.* Highly Stretchable, Knittable, Wearable Fiberform Hydrovoltaic
1771 Generators Driven by Water Transpiration for Portable Self-Power Supply and Self-Powered
1772 Strain Sensor. *Small* **20**, 2306318 (2024).
- 1773 114. Anys, M. & Weiler, M. Controls on Tree Transpiration Dynamics in an Urban
1774 Environment. Preprint at <https://doi.org/10.2139/ssrn.4805499> (2024).
- 1775 115. Bachofen, C. *et al.* Tree water uptake patterns across the globe. *New Phytol.* **242**, 1891–
1776 1910 (2024).



- 1777 116. Hu, Q. *et al.* Hydrovoltaic electricity generation induced by living leaf transpiration. *Nat.*
1778 *Water* **2**, 988–998 (2024).
- 1779 117. Hu, Q. *et al.* Hydrovoltaic electricity generation induced by living leaf transpiration. *Nat.*
1780 *Water* **2**, 988–998 (2024).
- 1781 118. Li, Z. *et al.* Polyaniline-Coated MOFs Nanorod Arrays for Efficient Evaporation-Driven
1782 Electricity Generation and Solar Steam Desalination. *Adv. Sci.* **8**, 2004552 (2021).
- 1783 119. Piao, X. *et al.* Water-evaporation induced electricity generation inspired by natural tree
1784 transpiration. *Sustain. Mater. Technol.* **39**, e00836 (2024).
- 1785 120. Zhang, J. *et al.* Paper-Based Hydroelectric Generators for Water Evaporation-Induced
1786 Electricity Generation. *Adv. Sci.* **10**, 2304482 (2023).
- 1787 121. Sudhir, S., Arunprasath, A. & Sankara Vel, V. A critical review on adaptations, and
1788 biological activities of the mangroves. *J. Nat. Pestic. Res.* **1**, 100006 (2022).
- 1789 122. Parida, A. K. & Das, A. B. Salt tolerance and salinity effects on plants: a review.
1790 *Ecotoxicol. Environ. Saf.* **60**, 324–349 (2005).
- 1791 123. Naseer, S. *et al.* Casparian strip diffusion barrier in *Arabidopsis* is made of a lignin
1792 polymer without suberin. *Proc. Natl. Acad. Sci.* **109**, 10101–10106 (2012).
- 1793 124. Liu, Y. *et al.* A fabric-based hydrovoltaic electricity generator with multi-component
1794 carbon black for sustainable energy output. *RSC Adv.* **14**, 18832–18837 (2024).
- 1795 125. Kumar, R., Tabrizzadeh, T., Chaurasia, S., Liu, G. & Stampelcoskie, K. Hydrovoltaic
1796 power generation from multiwalled carbon nanotubes. *Sustain. Energy Fuels* **6**, 1141–1147
1797 (2022).
- 1798 126. Yuan, W. *et al.* Scalable MXene/Sepiolite film-based hydrovoltaic generators with
1799 outstanding output power. *Chem. Eng. J.* **499**, 155952 (2024).



- 1800 127. Bae, J. *et al.* Towards Watt-scale hydroelectric energy harvesting by $Ti_3 C_2 T_x$ -based
1801 transpiration-driven electrokinetic power generators. *Energy Environ. Sci.* **15**, 123–135
1802 (2022).
- 1803 128. Beaton, G. C., Kumar, R., Neokleous, N., Liu, G. & Stampelcoskie, K. Gold nanoparticle
1804 decorated filter papers as hydrovoltaic devices. *Sustain. Energy Fuels* **6**, 4645–4651 (2022).
- 1805 129. Zhou, Z. *et al.* Self-powered TpPa/PAN membrane-based flexible hydrovoltaic sensor for
1806 real-time Congo red monitoring. *Sens. Actuators B Chem.* **432**, 137507 (2025).
- 1807 130. Ding, H. *et al.* Hydrovoltaic Effect Coupling with Capacitor Amplification: A Mode for
1808 Sensitive Self-Powered Electrochemical Sensing. *Anal. Chem.* **95**, 12595–12599 (2023).
- 1809 131. Lin, Y. *et al.* Evaporation-Driven Fabric for Synergistic Water-Electricity-Lithium
1810 Co-Production. *Adv. Mater.* **37**, e06956 (2025).
- 1811 132. Chen, X. *et al.* Spatially separated crystallization for selective lithium extraction from
1812 saline water. *Nat. Water* **1**, 808–817 (2023).
- 1813 133. Liu, C. *et al.* Lithium Extraction from Seawater through Pulsed Electrochemical
1814 Intercalation. *Joule* **4**, 1459–1469 (2020).
- 1815 134. Liu, Q. *et al.* Fully Printable Manufacturing of Miniaturized, Highly Integrated, Flexible
1816 Evaporation-Driven Electricity Generator Arrays. *Adv. Sci.* **12**, 2413779 (2025).
- 1817 135. Wang, L., Zhang, W. & Deng, Y. High-voltage hydrovoltaic generator based on
1818 micro/nano multi-scale superhydrophilic SiO_2 @activated carbon with enhanced capillary
1819 infiltration performance. *Mater. Horiz.* **12**, 8724–8733 (2025).
- 1820 136. Gao, W. *et al.* Fully integrated wearable sensor arrays for multiplexed in situ perspiration
1821 analysis. *Nature* **529**, 509–514 (2016).
- 1822



1823

1824

1825

1826

1827

1828

Open Access Article. Published on 09 April 2026. Downloaded on 4/11/2026 10:06:12 PM.
This article is licensed under a Creative Commons Attribution-NonCommercial 3.0 Unported Licence.



Data availability

This review article did not generate or analyze any new datasets. All data discussed are derived from previously published studies and are cited in the article and its references. Any datasets underlying the cited works are available from the corresponding original publications and, where applicable, from the repositories listed by those authors.

